JGR Solid Earth

RESEARCH ARTICLE
10.1029/2019JB018440

Key Points:
- 3D fine-scale geometry and kinematics of the 2016–2017 Central Italy Sequence by HypoDD locations of data produced in monitoring environment
- Space-time evolution of the seismic activity and its relation with a shallow shear zone bounding the system at depth
- Focus on faults segmentation and role of the preexisting compressional structures in modulating the extensional deformation pattern

Supporting Information:
- Supporting Information S1

Correspondence to:
M. Michele,
maddalena.michele@ingv.it

Citation:
Michele, M., Chiaraluce, L., Di Stefano, R., & Waldhauser, F. (2020). Fine-scale structure of the 2016–2017 Central Italy seismic sequence from data recorded at the Italian National Network. *Journal of Geophysical Research: Solid Earth*, *125*, e2019JB018440. https://doi.org/10.1029/2019JB018440

Received 25 JUL 2019
Accepted 18 MAR 2020
Accepted article online 23 MAR 2020

Fine-Scale Structure of the 2016–2017 Central Italy Seismic Sequence From Data Recorded at the Italian National Network

M. Michele[1], L. Chiaraluce[1], R. Di Stefano[1], and F. Waldhauser[2]

[1]Istituto Nazionale di Geofisica e Vulcanologia, Rome, Italy, [2]Lamont-Doherty Earth Observatory, Columbia University, New York, NY, USA

Abstract We explore the three-dimensional structure of the 2016–2017 Central Italy sequence using ~34,000 $M_L \geq 1.5$ earthquakes that occurred between August 2016 and January 2018. We applied cross-correlation and double-difference location methods to waveform and parametric data routinely produced at the Italian National Institute of Geophysics and Volcanology. The sequence activated an 80 km long system of normal faults and near-horizontal detachment faults through the M_W 6.0 Amatrice, the M_W 5.9 Visso, and the M_W 6.5 Norcia mainshocks and aftershocks. The system has an average strike of N155°E and dips 38°–55° southwestward and is segmented into 15–30 km long faults individually activated by the cascade of $M_W \geq 5.0$ shocks. The two main normal fault segments, Mt. Vettore-Mt. Bove to the North and Mt. della Laga to the South, are separated by an NNE-SSW-trending lateral ramp of the Sibillini thrust, a regional structure inherited from the previous compressional tectonic phase putting into contact diverse lithologies with different seismicity patterns. Space-time reconstruction of the fault system supports a composite rupture scenario previously proposed for the M_W 6.5 Norcia earthquake, where the rupture possibly propagated also along an oblique portion of the Sibillini thrust. This dissected set of normal fault segments is bounded at 8–10 km depth by a continuous 2 km thick seismicity layer of extensional nature slightly dipping eastward and interpreted as a shear zone. All three mainshocks in the sequence nucleated along the high-angle planes at significant distance from the shear zone, thus complicating the interpretation of the mechanisms driving strain partitioning between these structures.

1. Introduction

The seismic sequence that occurred in Central Italy in 2016–17 is the most important sequence since 1980 when a M_W 6.9 struck the Irpinia region in the Southern Apennines (Boschi et al., 1990 and references therein). The sequence started in the summer of 2016 and is characterized by a succession of moderate-to-strong extensional earthquakes that occurred near the villages of Amatrice, Visso, and Norcia. These villages, and other villages nearby, were completely devastated, causing 299 fatalities and leaving more than 20,000 people homeless (Galli et al., 2016). The first earthquake near the medieval village of Amatrice occurred on 24 August with M_W 6.0 and caused the death of 299 people, being unfortunately occurred at night (at 01:36 UTC). Faults activated in the 2 years following the Amatrice mainshock reached 80 km of length along strike of the normal fault system (Figure 1). This is a very active sector of the Central-Northern Apennines fault system as revealed by the occurrence of a large series of historical earthquakes with $M_W \geq 6.0$, starting from the 13th century c. e. (Rovida et al., 2019). The instrumentally recorded seismic moment release has been similarly high.

The Amatrice-Visso-Norcia sequence (AVN) is confined by two other fault systems both recently activated by a series of $5 < M_W \leq 6.1$ earthquakes: Colfiorito 1997 to the north (Chiaraluce et al., 2003) and L'Aquila 2009 to the south (Valoroso et al., 2013). These sequences belong to a unique 150 km long normal fault system composed by individual contiguous and/or sub parallel, 10–30 km long, SW-dipping fault segments. Their static and dynamic interaction (Cocco et al., 2000; De Natale et al., 2011; Hernandez et al., 2004; Lavecchia et al., 2012; Mildon et al., 2017; Nostro et al., 2005; Pace et al., 2014; Papadopoulos et al., 2017; Pino et al., 1999; Verdecchia et al., 2018) as well as their interference with compressional structures formed during the previous tectonic phase is still debated (Chiaraluce et al., 2005, Chiaraluce et al., 2011; Chiaraluce, Di Stefano, et al., 2017 Scognamiglio et al., 2018; Buttinelli et al., 2018; Bonini et al., 2019).

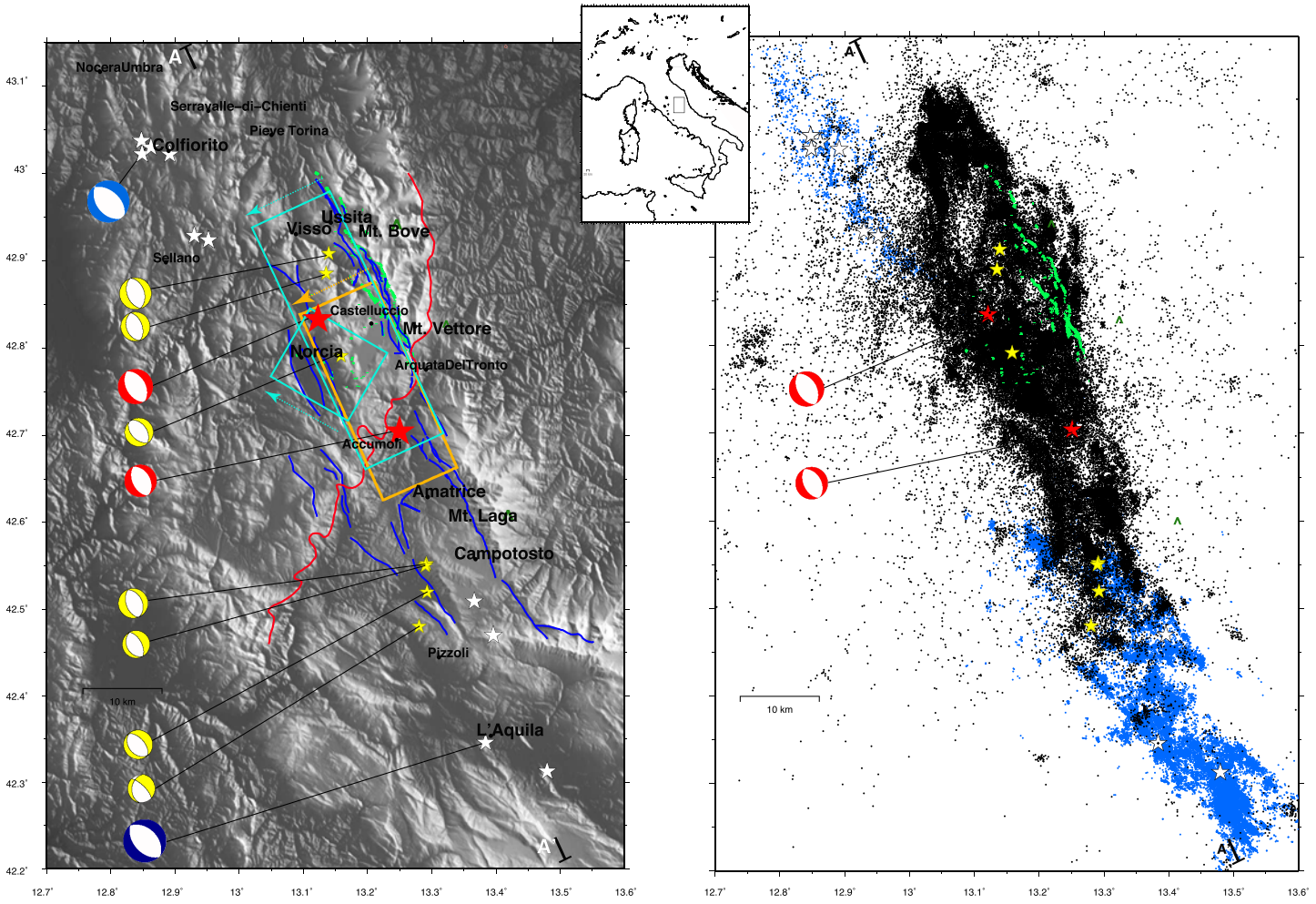

Figure 1. Left: map view of the study area. Green lines represent surface ruptures (Pucci et al., 2017) while the blue lines are the mapped normal faults (after Pucci et al., 2017). The red line is the Sibillini Thrust (ST); focal mechanisms of the events with $M_W \geq 5.0$ are reported. The orange rectangle represents the surface projection of the fault plane for the Amatrice earthquake (Tinti et al., 2016). The cyan boxes are the Norcia M_W 6.5 slip for the main fault, and the secondary fault; colored arrows show the direction of immersion (Scognamiglio et al., 2018). Right: light blue dots to NW correspond to 1997 Colfiorito seismic sequence earthquakes (Chiaraluce et al., 2003); light blue dots to SE correspond to 2009 L'Aquila seismic sequence earthquakes (Valoroso et al., 2013); black dots correspond to AVN seismic sequence earthquakes, relocated with NonLinLoc code; focal mechanisms of the events with $M_W \geq 6.0$ are reported. Both of the panels: for Colfiorito and L'Aquila sequences, white stars are events with $M_W \geq 5$; for AVN sequence, yellow stars are events with $5 \leq M_W < 6$; red stars are events with Mw $\geq$ 6.

The AVN sequence started with the M_W 6.0 Amatrice earthquake (hereinafter AM) on 24 August 2016 at 01:36 (UTC) close to the town of Amatrice at a shallow hypocentral depth (7.93 km; Michele et al., 2016; Tinti et al., 2016), causing intense ground shaking and a first evidence of centimeter-scale surface breakage along the Monte Vettore normal fault outcrop (Pucci et al., 2017). Following 2 months of continuous aftershocks activity, another segment failed in the M_W 5.9 Visso Earthquake (hereinafter VI) in the north-western portion of the aftershock area on 26 October 2016 at 19:18 (UTC). Four days later, the strongest event of the sequence with M_W 6.5 occurred close to Norcia (hereinafter NO 30 October 2016 06:40 UTC), roughly in the middle between towns of Amatrice and Visso. A series of four additional moderate magnitude earthquakes, all with extensional kinematics, hits the southern termination of the system with moment magnitudes ranging between 5.0 and 5.5 in the Campotosto area (Figure 1). The cascade type evolution of the sequence typically observed along this sector of the Apenninic chain (Chiaraluce et al., 2004; Papadopoulos et al., 2017; Verdecchia et al., 2018; Xu et al., 2017) prevented additional human losses after the AM earthquake, because many people had already abandoned their habitations.

A preliminary analysis of the seismic data demonstrated that each mainshock ruptured different, slightly off-axis portions of an SW dipping normal fault with strikes NW-SE trending parallel to the axis of the Apennines mountain belt (Chiaraluce, Di Stefano, et al., 2017), consistent with the known northeast-trending tectonic extension at a rate of 3 mm/year of the inner Apennines (Serpelloni et al., 2005). The geologic structures responsible for the AVN sequence are placed in a sector in between the Umbria-Marche and the Latium-Abruzzi geologic domains (Figure 1). Initial absolute locations of the AVN aftershocks (Michele et al., 2016; Chiaraluce, Di Stefano, et al., 2017) revealed the broad scale geometry of this composite fault system made of two main distinct Quaternary NW-trending normal fault segments, the Mt. Vettore-Mt Bove (VBFS) to the north and the Mt. della Laga to the south, separated by the Pliocene Sibillini thrust (ST; Centamore & Rossi, 2009; Calamita et al., 2012; Di Domenica et al., 2014; Figure 1). This latter structure has a curved shape defined at regional scale by an NNW-SSE-trending frontal ramp and an NNE-SSW-trending oblique ramp, respectively, to the north and south of Mt. Vettore where it crosses the AVN activated fault segments (Chiaraluce, Di Stefano, et al., 2017). The ST juxtaposes the Triassic-Miocene carbonate succession on Tertiary succession composed by Oligocene-Miocene marls (Scaglia Cinerea and Marne con Cerrogna Fms.) and Messinian siliciclastic deposits (Laga Fm.). The role of the ST structure in constraining the extensional deformation, mainly occurring along NW-trending normal faults segments, is still debated (Tinti et al., 2016; Chiaraluce, Di Stefano, et al., 2017, Pizzi et al., 2017; Bonini et al., 2019), as well as the nature of the normal faults possibly reutilizing preexisting steep ramps formed during the late Pliocene compressive phase (Buttinelli et al., 2018; Chiarabba et al., 2018). In addition to this, Scognamiglio et al. (2018) suggested an active role of a portion of the compressional structure, proposing a composite rupture model for the strongest Norcia earthquake: a main NW-trending normal fault segment, coinciding with the extensional VBFS, and a secondary plane coinciding with the deep portion of the NNE-trending sector of the ST, implying at depth a kinematic inversion of the thrust ramp (see Figures 6a and 6b). However, coseismic surface ruptures, associated with the NO event, are solely located on the NW trending normal fault splays of the VBFS over a length of ~22 km and an average surface displacement of ~0.44 m (peak ~2.10 m; Villani et al., 2018).

The comparison between the subsurface geology based on seismic reflection profiles and geological data, with the seismological data, in terms of aftershocks distribution (Porreca et al., 2018) has shown that the majority of seismicity is confined within the sedimentary succession, as suggested by Chiaraluce, Barchi, et al. (2017) by analyzing both the background activity and the 1997 and 2009 seismic sequences. It is interesting to note that the entire normal fault system, confined within the first 8 km of the upper crust, is bounded below by a shallow east-dipping and ~2 km thick layer where small events and a series of moderate aftershocks (≈Mw 4) occur, possibly decoupling the upper and lower crusts and contributing to the loading of the higher angle faults above (Chiaraluce, Di Stefano, et al., 2017; Vuan et al., 2017). The correlation between this seismicity, the underlying basement position (from 8 to 11 km of depths), and the abrupt cuff-off of seismicity at depth are still to be understood. In this context, the reconstruction of the fine scale AVN fault system geometry and kinematics based on aftershocks distribution and focal mechanisms distribution offer important contributions to a better understanding of diverse hazard scenarios in terms of evolutionary trends of the extensional seismic sequences, including fault segmentation, the occurrence of large aftershocks at short time intervals, and fault interaction.

The analysis of strong motion and broad band data finalized to the study of coseismic slip distribution, rupture history, and directivity of the largest ($M_W > 4.4$) events of the AVN sequence (Tinti et al., 2016; Chiaraluce, Di Stefano, et al., 2017; Calderoni et al., 2017; Pizzi et al., 2017; Scognamiglio et al., 2018) reveals a high degree of complexity and a consistent along strike propagation independent of the size of the earthquakes. These seem to be persistent features of Apenninic normal faulting earthquakes, previously observed also for the strongest shocks of the 1997 (Cultrera et al., 2009) and 2009 (Calderoni et al., 2011) sequences, together with the frequently observed along strike seismicity migration (Chiaraluce, 2012).

In this paper, we present double difference (hereinafter DD; Waldhauser & Ellsworth, 2000) relative locations of the AVN mainshocks-aftershocks sequence using the data set described in Chiaraluce, Di Stefano, et al. (2017). We extended the catalog to include smaller magnitudes (all events with $M_L \geq 1.5$) and a longer observation period (24 August 2016 to 18 January 2018). We used *P* and *S* wave arrival times manually picked by analysts of the National Institute of Geophysics and Volcanology (INGV) seismic monitoring room. We combined the pick data with cross-correlation delay time measurements in our DD analysis.

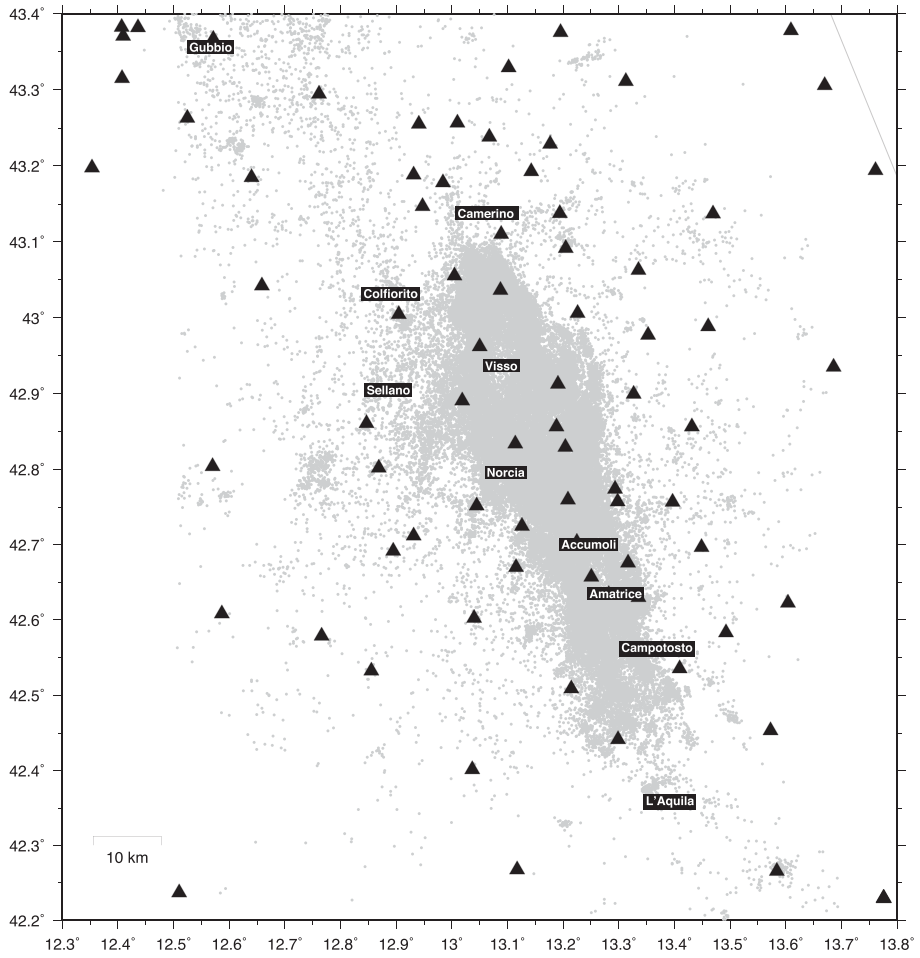

Figure 2. Map view of the RSN seismic network. Black triangles indicate the sites of the permanent and mobile stations of the Italian National Network managed by the INGV. Gray dots in background are the AVN sequence earthquakes.

The resulting catalog consists of ~34,000 events whose high-resolution locations were used for describing the fault system structure and seismicity pattern of the sequence, discussing diverse mechanical comportment of each activated sector as well as the role of the interconnecting fault segmentation.

Chiaraluce, Di Stefano, et al. (2017), in their probabilistic analysis of earthquakes distribution using hand-picked data, revealed the first-order image of a continuous fault system from south to north, characterized by segmentation, interpreted as a unique fault system extending from south of Amatrice up to the area north of the village of Visso, embedded at depth by a subhorizontal seismicity layer. Here, we present relocation results with significantly improved hypocenter resolution compared to Chiaraluce et al. (2017), allowing us to investigate minor anti and synthetic structures that were not visible before, the thickness of fault zones, the mainshocks positions within the active fault system, and the interaction of the basal layer with the fault system structures and with the hosting geology formations. Finally, we discuss in detail the southern and northern termination of the AVN sequence and their structural relationship with the overlapping previous sequences of Colfiorito 1997 and L'Aquila-Campotosto 2009.

2. Earthquakes Location

The seismic sequence was recorded in real time within 80 km of the epicentral area by about 74 permanent three components seismic stations of the Italian National Seismic Network (Figure 2). Additional 24 stations were temporarily deployed soon after the AM mainshock, transmitting data in real time to the Italian national acquisition center managed by INGV and placed in Rome. We started our relocation process

Table 1
Conversion Between Monitoring Room Data Quality Classes, Uncertainties in Seconds, and Input Weights for the HypoDD Inversion

Data quality	0	1	2
Uncertainty (s)	0.1	0.3	0.6
DD weight	1	0.5	0.2

from the data processed by the INGV seismic monitoring system which firstly automatically detects the earthquake, picks and binds arrival times, and locates the event. Then, downstream of this automatic procedure, most of the *P* and *S* wave arrival time are manually revised by the analysts working 24/7 in the monitoring room. In this study, by improving the relative arrival times by means of cross correlation and double-difference analysis, we tested the potential of these semiautomatically produced data in resolving the detailed structures and geometry of active faults. The great advantage of using these data as starting point is that they are available in near real-time through open access web services.

We use a two-step procedure to obtain a high-resolution catalog. We first improved on the INGV routine absolute locations for all events with $M_L \geq 1.5$ that occurred in the study area between August 2016 and January 2018, using the grid search methods similar to Chiaraluce, Di Stefano, et al. (2017). We then improved relative locations by applying the DD relative location procedure to the catalog picks and precise phase delay times measured from waveform cross correlation.

2.1. Absolute Earthquake Location Using Grid Search

To improve the absolute locations in the starting earthquake catalog available from the INGV (http://cnt.rm.ingv.it), we used the NonLinLoc code (Lomax et al., 2001). The NonLinLoc algorithm is based on a probabilistic approach that minimizes the L1 norm of the travel time residuals in order to provide a complete solution to the location problem, including information on uncertainty.

We used the same 1-D gradient *P* and *S* wave velocity models (after Carannante et al., 2013) used in Michele et al. (2016) and Chiaraluce, Di Stefano, et al. (2017). In order to reduce systematic travel time biases caused by a simplified 1D velocity model and to account for the lack of receiver side information about the shallower portion of the crust, we included the static station corrections proposed for each station by Chiaraluce et al., 2017.

Arrival time pick quality reported in the INGV bulletin is converted to data uncertainty for use with NonLinLoc as indicated in Table 1. The highest quality data (0 quality) have picking uncertainty lower than 0.1 s while picked data with an uncertainty greater than 0.6 s are discarded. After the selection, the dataset consists of 612,207 *P* and 465,693 *S* onset readings.

We report in Figure 1 the epicenters of the 34,436 earthquakes (black dots) located with the NonLinLoc code obeying to the following a priori and a posteriori quality criterion: root mean square (RMS) equal or less than 0.5 s, horizontal and vertical formal error equal or less than 1.5 and 3.0 km, respectively, at least 10 onset picks (*P* or *S*), and an azimuthal gap less than 180°.

2.2. Relative Earthquake Location Using Double Differences

By refining the relative positions of nearby earthquakes, the fine structure of the seismicity is enhanced, allowing to better image the geometry of the three-dimensional fault system and the structure of active faults. The high density of recorded earthquakes within the AVN sequence allows for application of the double-difference method (Waldhauser & Ellsworth, 2000) to the high-quality dataset of absolute locations described above.

When the hypocentral distance between two seismic events is small with respect to the source-receiver distance and to the scale-length of velocity heterogeneity (De Landro et al., 2015; Waldhauser & Ellsworth, 2000) and their focal mechanisms are similar, the ray paths connecting the source region with a common station are similar, and as a consequence, their waveforms are similar. In this case, cross-correlation can measure phase delay times with high precision by aligning the *P* and *S* wave trains (Poupinet et al., 1984).

We applied a time domain cross-correlation method (Schaff et al., 2004; Schaff & Waldhauser, 2005) to seismograms of all pairs of events separated by 3 km or less and recorded at common stations. This method allows to compute differential travel times at subsample precision (Fréchet, 1985; Poupinet et al., 1984; Schaff et al., 2004). When no picks are available for initial alignment, travel times are computed in the 1D velocity model used for location. Similar to the L'Aquila study of Valoroso et al. (2013), the seismograms were filtered in the 1–15 Hz frequency range using a four pole, zero phase band-pass Butterworth filter.

The correlation measurements were performed on 0.7 s long window for *P* waves and 1 s windows for *S* waves. We retain all measurements with correlation coefficients greater than 0.7 resulting in a total of ~4.4 million *P* and ~1.1 million *S* wave delay times. We selected the cross-correlation coefficient threshold based on previous experience (e.g., Chiaraluce et al., 2007; Schaff et al., 2002; Schaff & Waldhauser, 2005; Valoroso et al., 2013) with the goal to optimize the quality of these measurements for relocation purposes.

A comparison between delay time differences determined with cross-correlation and those from arrival time picks shows median absolute deviations of ~0.1 s for *P* and *S* waves, including all cross-correlation data with coefficients >0.7 (Figures 3a and 3b). Most of the differences can be attributed to uncertainties in the arrival time picks, especially for higher correlation coefficient data that are typically precise to a few milliseconds. Waveform similarity decays with increasing interevent distance due to the increasing effect of differences in ray paths, as illustrated in Figure 3c. In order to evaluate how cross-correlation coefficients vary across the study area, we show curves for several subregions. Results for *P* cross-correlation coefficients are robust throughout the area, while *S* coefficients are generally lower in the northern part.

We combined the cross-correlation delay time measurements with delay times computed from picks for event pairs separated by less than 8 km and recorded within 200 km and simultaneously inverted for relative locations by using the double difference location code HypoDD (Waldhauser, 2001; Waldhauser & Ellsworth, 2000). The DD algorithm is based on an iterative least squares' procedure minimizing the differential time residuals for pairs of earthquakes recorded at common stations by adjusting the vector connecting their hypocenters (Waldhauser & Ellsworth, 2000). We invert all differential travel times that link together every event to an optimized selection of up to 30 neighboring events within 8 km distance.

In order to handle the computational load, we subdivided the entire dataset in 18 rectangular boxes, orthogonal to and centered on the mean strike of the seismic sequence. Each box includes a maximum of 6,000 earthquakes and overlaps with neighboring boxes by 50% in NW-SE extension. HypoDD is run separately on each box, using 25 iterations of damped and dynamically weighted least square inversions. Finally, the DD relative locations from all boxes were combined into a single catalog, with the weighted mean of hypocenters taken for the same events that are located in the overlapping regions (Waldhauser & Schaff, 2008).

The final double-difference catalog includes 33,982 events occurring between 24 August 2016 and 18 January 2018. It shows a significant reduction in RMS with respect to the NonLinLoc catalog (Figure 3d). Formal errors for well-constrained subsets of the catalog were computed from the full covariance matrix using Singular Value Decomposition (SVD; see Waldhauser & Ellsworth, 2000 for details). The mean value of horizontal errors distribution is 110 m in east-west direction and 120 m north–south, while the mean value of vertical errors is 162 m (Figure 3e).

In Table 2, we compare the mainshock absolute locations derived with NonLinLoc with those derived with HypoDD. The mean epicentral distance between the two locations is ~600 m, and the mean depth difference is ~1.4 km, generally within the location uncertainty of the NonLinLoc locations. DD depths are generally shallower and significantly so for the Amatrice event, but these depths are consistent with structures activated by aftershocks and observed at the surface. They are also consistent with *S*-*P* times of nearby smaller events recorded at the stations placed above the hypocenters. Previous studies also place the hypocenter above and away from the subhorizontal shear zone (Chiaraluce et al. 2017; Chiarabba et al., 2018).

DD hypocenters of the $M_W > 5$ events are well constrained through robust relative *P* and *S* travel time links to a large number of neighboring smaller events which tend to be strongly constrained by cross correlation measurements. We note here that because the large events are mainly controlled by phase onset picks during the double-difference inversion of the combined data set, these locations image the nucleation location of the event. Locations of smaller events constrained mainly by cross-correlation data represent the maximum moment release (see Waldhauser & Ellsworth, 2000). For small events ($M_L \sim < 2.5$), the difference between the two locations on the rupture surface may not be resolvable.

3. Location Results

We first analyze the evolution of the seismicity pattern including the multiple activation of the fault segments and the progression of the seismic activity along a shear zone bounding at depth the entire fault system, by examining space-time diagrams of the seismic activity (section 3.1).

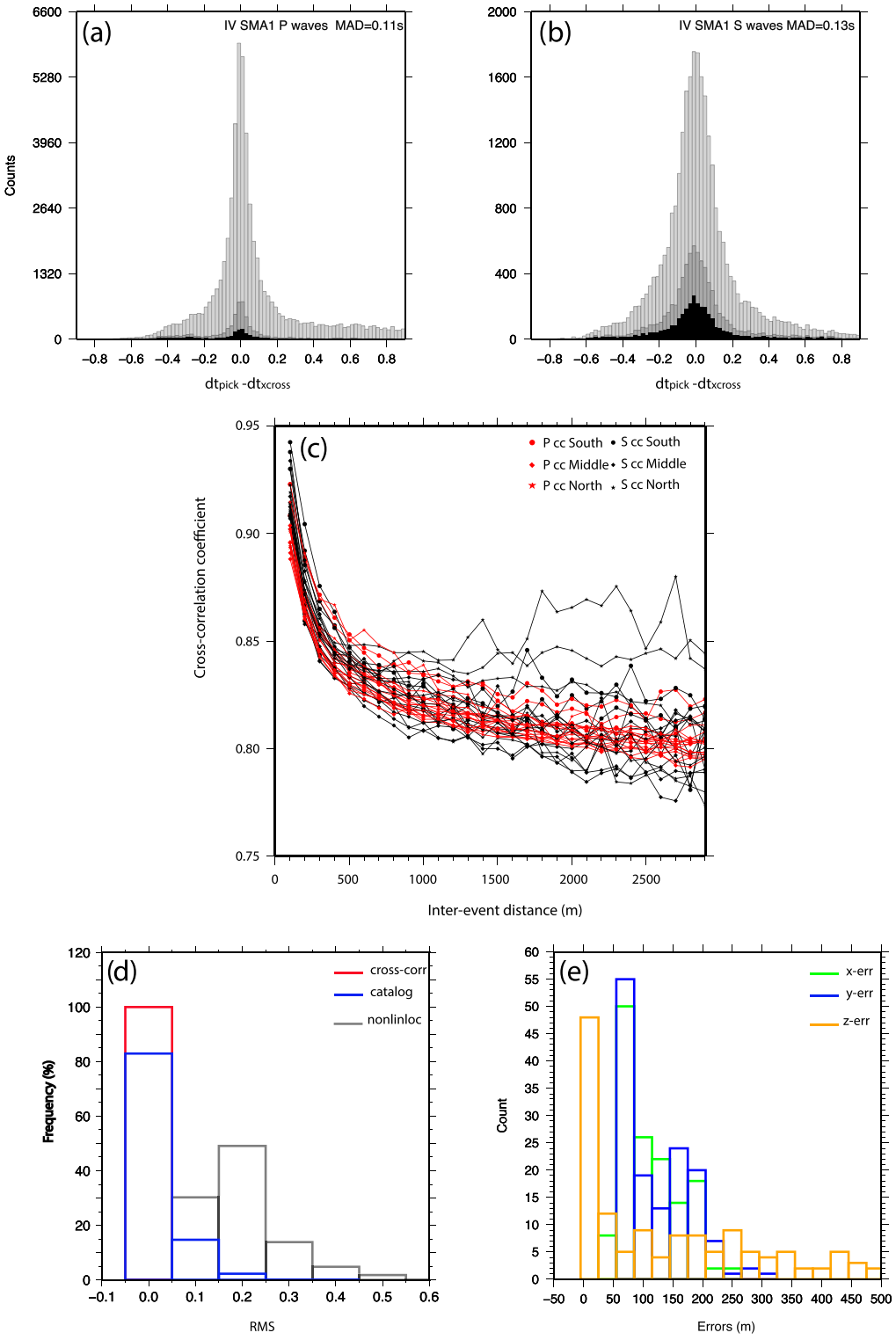

Figure 3. (a, b) Histograms of differences between pick and cross-correlation *P* and *S* wave delay times for corresponding pairs of events, shown for three correlation coefficient (Cf) cut-off values (0.7 in light gray, 0.8 in gray and 0.9 in black); (c) cross-correlation values versus interevent separation distance for *P* (red) and *S* wave (black). Different markers correspond to three different geographical macro areas, each of them containing six boxes and so six lines. Each point represents an average over 50 m bins of interevent values for both *P* and *S* waves, for all the stations; (d) histogram showing the RMS distribution (in seconds) for starting absolute locations (gray) and for DD relative locations from catalog data (blue) and cross-correlation data (red); (e) histogram showing the relative locations errors in the three components (x, y, and z), computed from the full covariance matrix of a subset of 150 events.

Table 2
$M_W \geq 5.0$ Earthquakes Absolute and Relative Location Parameters

Date	Origin time	Lat. (°)	Lon. (°)	Depth (km)	Mag (M_W)
2016-08-24	01:36:32.702	42.70409	13.25100	7.935	6.0
	01:36:32.760	42.71233	13.25269	4.651	
2016-08-24	02:33:29.792	42.79128	13.15830	6.569	5.3
	02:33:29.835	42.79820	13.16050	4.8705	
2016-10-26	17:10:37.150	42.88592	13.13498	4.183	5.4
	17:10:37.160	42.89190	13.13750	3.462	
2016-10-26	19:18:06.748	42.90870	13.13917	2.443	5.9
	19:18:06.720	42.91020	13.14120	2.473	
2016-10-30	06:40:18.099	42.83502	13.12124	7.321	6.5
	06:40:18.155	42.83860	13.12600	5.782	
2017-01-18	09:25:40.955	42.55199	13.29135	8.746	5.1
	09:25:41.020	42.55760	13.29600	7.872	
2017-01-18	10:14:10.733	42.55008	13.28979	8.322	5.5
	10:14:10.670	42.55300	13.28700	7.725	
2017-01-18	10:25:24.370	42.51957	13.29224	9.717	5.4
	10:25:24.420	42.52385	13.28828	8.381	
2017-01-18	13:33:37.421	42.48006	13.28011	10.168	5.0
	13:33:37.400	42.48551	13.27768	9.433	

Note. Date (year-month-day), Origin Time (hour:minute:second), Lat (latitude), Lon (Longitude), Depth (Hypocentral depth), Mag (magnitude). The underlined parameters are those of the relative HypoDD locations.

Then we make use of our relocated catalog drawing a set of 35 cross-sections orthogonal to the mean strike of the main faults (N60°E oriented) to analyze the fault system geometry. We separated the description of the areas hit by the mainshocks (sections 3.2–3.5) plus the southern and northern faults termination described by looking at longitudinal sections (section 3.6).

3.1. Space-Time Evolution of the Sequence

We use a space time diagram, centered on the nucleation point of the M_W 6.0 AM earthquake (red star at 0 distance), to describe the evolution of seismicity (Figure 4). The AM early aftershocks distribution, starting from the Accumoli village, spreads bilaterally; 15 km northward toward Castelluccio-Vettore, where 1 hr after the mainshock, a M_W 5.4 overstepping the Sibillini Thrust occurred, and 15 km southward toward Campotosto, where the aftershocks are less frequent (Figure 4a). This distribution agrees with the bilateral rupture directivity proposed for the AM shock (Calderoni et al., 2017; Tinti et al., 2016). Two months later, another fault segment, about 20 km long, reaching from Mt. Bove-Visso to Camerino, was activated in the north-western portion of the area by the M_W 5.9 Visso earthquake (VI).

The activation of this area, explored by vertical sections 25–29 in Figure 5c, represents a significant change in the space-time evolution of the AVN sequence. Before the Visso earthquake on 26 October 2016, only little seismic activity was observed at this latitude toward the Visso hypocenter at the northern termination of the fault system. Seismic release was progressively decreasing in the whole area after the Amatrice M_W 6.0 earthquake on 24 August. Then on 26 October 2016, a M_W 5.4 (green star in Figures 4a and 4b), presumably a foreshock, preceded, by 2 hr, the Visso M_W 5.9 (yellow star), which struck the region 3 km south of the village of Visso. The Visso earthquake reactivated the southern portion of the normal fault system, reaching the town of Norcia. It activated for the first time the northern portion of the fault system toward Camerino (see Figures 1 and 4). The VI aftershocks occur predominantly to the north of the mainshock, consistent with the strong unilateral rupture directivity toward north obtained for this event (Chiaraluce, Di Stefano, et al., 2017).

Four days after the Visso earthquake, on the 30 October, the strongest event of the sequence with M_W 6.5 occurred close to Norcia (NO; red star in Figure 4), roughly in the middle between Amatrice and Visso. It is evident that the NO earthquake nucleated in an area already seismically active. A comparison between Figure 4a, which shows seismicity associated with the normal faults, and Figure 4c, which shows the shear zone activity, indicates that in October 2016, the seismicity moved from the shear zone to the normal fault system.

Finally, 20 days after the M_W 6.5 NO earthquake, we observed an increase of the seismic activity in the southern portion of the system nearby the Campotosto area. This activity could be considered as a foreshock sequence preceding the occurrence of the four $5.0 \leq M_W \leq 5.5$ of 18 January 2017, all with extensional kinematics. We will see that these events reactivated a portion of the same fault activated by other two moderate magnitude earthquakes during the 2009 L'Aquila earthquake (see yellow stars at the right end of Figure 4). It is important to note that immediately after the M_W 6.0 AM earthquake this southern termination only showed sparse seismicity with no clear faults identifiable.

In order to evaluate and compare the seismicity related to the subhorizontal shear zone (Michele et al., 2016; Chiaraluce, Di Stefano, et al., 2017 Vuan et al., 2017) and that related to the normal faults, we separately plot all the events occurring within +/−1.5 km from the variable top of its surface (Figure 4c) and those above (Figure 4b). We note that the two patterns (Figures 4b and 4c) are different. The seismic release along the shear zone occurs in burst that activates different parts of the shear zone modulated by the mainshock occurrences, but eventually occupy the entire slip surface. Similarly, the release related to the activation of the normal faults is also modulated by the mainshocks. Several areas in the pattern of the shallower

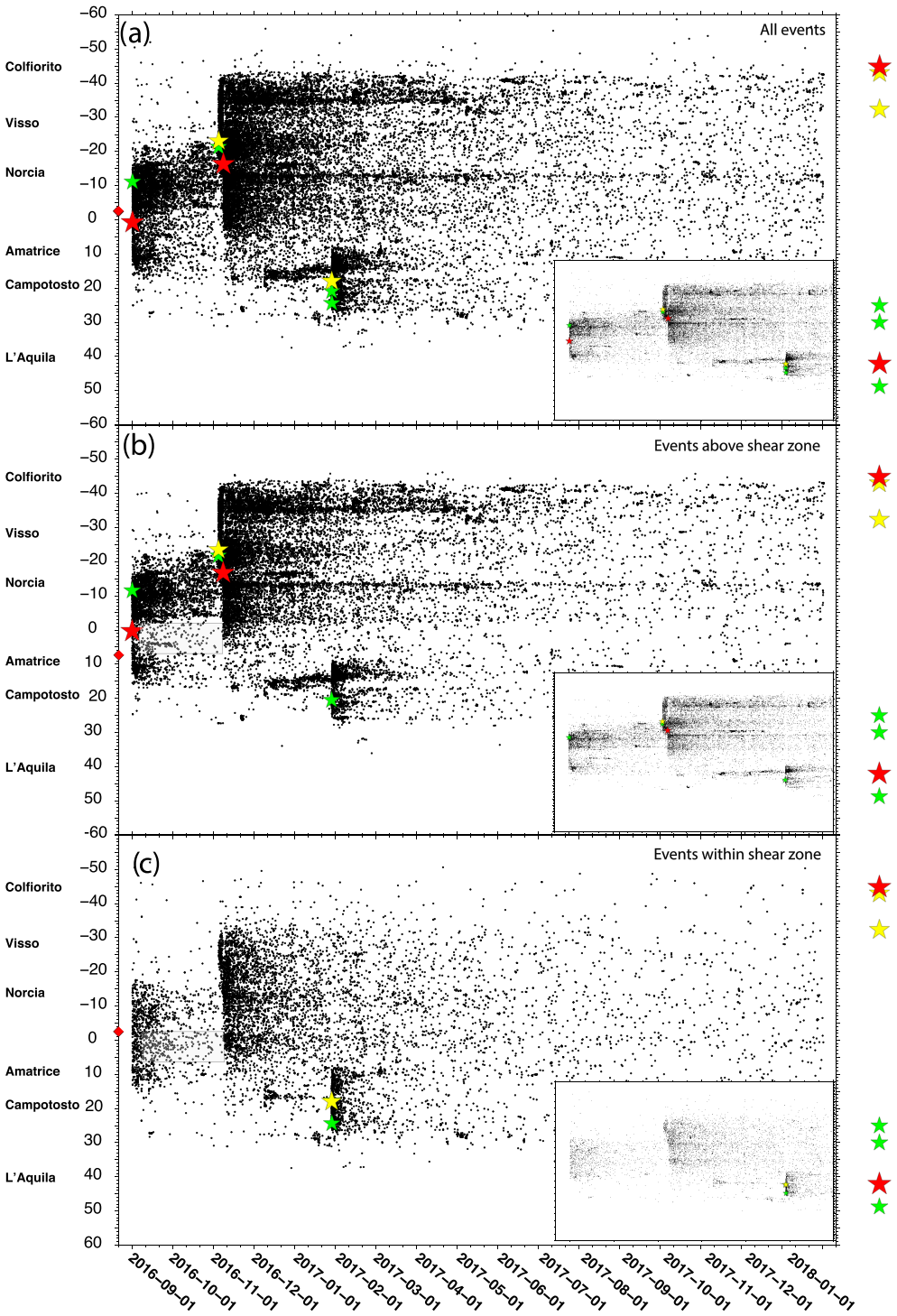

Figure 4. Space-time evolution of the Central Italy 2016–2017 sequence. In the three panels, on the x-axis, we report date, on the y-axis, we report the along-strike distance from the M_W 6.0 Amatrice location. Black dots are the earthquakes with $M_W < 5.0$; green stars are earthquakes with $5.0 \leq M_W < 5.5$; yellow stars are earthquakes with $5.5 \leq M_W < 6.0$; red stars are $M_W \geq 6.0$ earthquakes. On the left, the locations of nearby villages are indicated; on the right, the locations of all $M_W \geq 5.0$ in the Colfiorito and L'Aquila sequence. The red diamond corresponds to the intersections with the Sibillini thrust. Top panel (a) reports all the earthquakes without selection in depth; middle panel (b) reports only earthquakes having depth shallower than the variable top of the shear-zone (SZ); bottom panel (c) represents only earthquakes having depth deeper than the variable top of the SZ.

seismicity show along strike seismic quiescence, as for example following the AM mainshock (from −3 km to 5 km in Figure 4b). The Campotosto area suggests a coupling between the two patterns. We will see that this may be due to the shallow seismicity that flattens in this area with depth. We note that the series of $M_W > 5$ events in January 2017 (green and yellow stars in Figure 4a), differently from all the major mainshocks, here in fact nucleate along the shear zone itself.

3.2. Campotosto Area

Moving along strike from SE to NW (sections 1–9 in Figure 5b), we first observe the reactivation of the northern portion of the Mt. Gorzano fault, the southern sector of which, named Campotosto, was previously activated in 2009 during the L'Aquila sequence (Chiaraluce et al., 2011; Valoroso et al., 2013). Aftershocks in sections 1–6, located between 4 and 15 km depth and 0.5–1.0 km wide, indicate a change in fault geometry; kinked in the southern part with dip change at around 7 km depth, and planar dipping 35°–40° in the north.

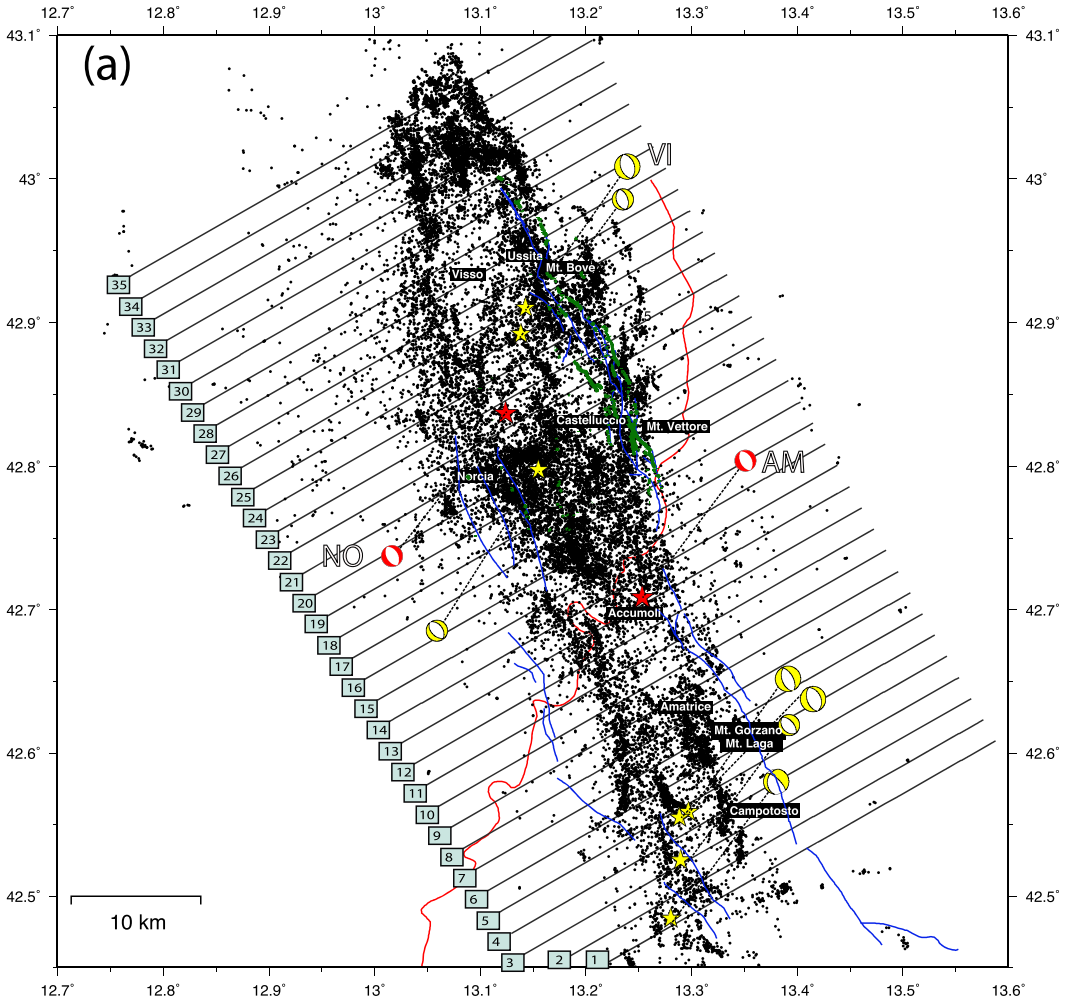

Figure 5. (a) Map view of the relocated aftershocks (black dots). Red stars are earthquakes with $M_W \geq 6.0$; yellow stars are earthquakes with $5.0 \leq M_W \leq 6.0$. The blue lines are normal faults traces, the red line is the trace of the Sibillini Thrust, and the green lines are the surface ruptures reported by Pucci et al. (2017). Beach balls represent focal mechanisms of the events with $M_W \geq 5.0$. Dark gray lines show the locations of the vertical cross sections shown in Figures 5b and 5c with numbers corresponding to numbers in the lower left corner of each section. (b, c) Cross section along profiles shown in (a). Each cross section includes earthquakes that occur within 1 km of the profile. Black dots are the AVN aftershocks along the vertical sections oriented orthogonally to the strike (150°) direction and centered on the M_W 6.5 NO. Yellow stars are the $5.0 \leq M_W < 6.0$ earthquakes while red stars are the $M_W \geq 6.0$ earthquakes, both with corresponding focal mechanisms shown. Blue segments are normal faults, red segments are the ST trace, and the green segments are surface ruptures (Pucci et al., 2017).

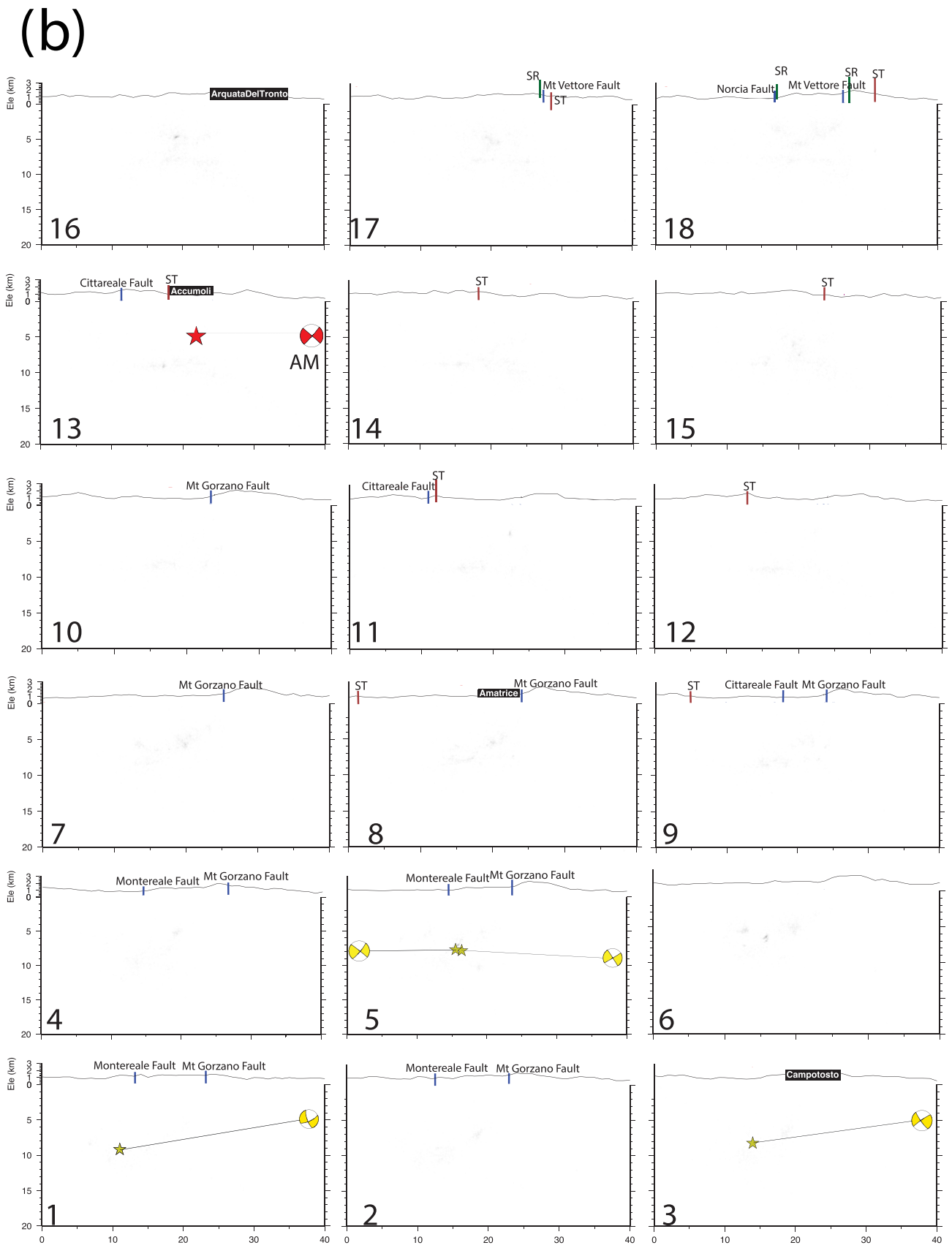

Figure 5. (continued)

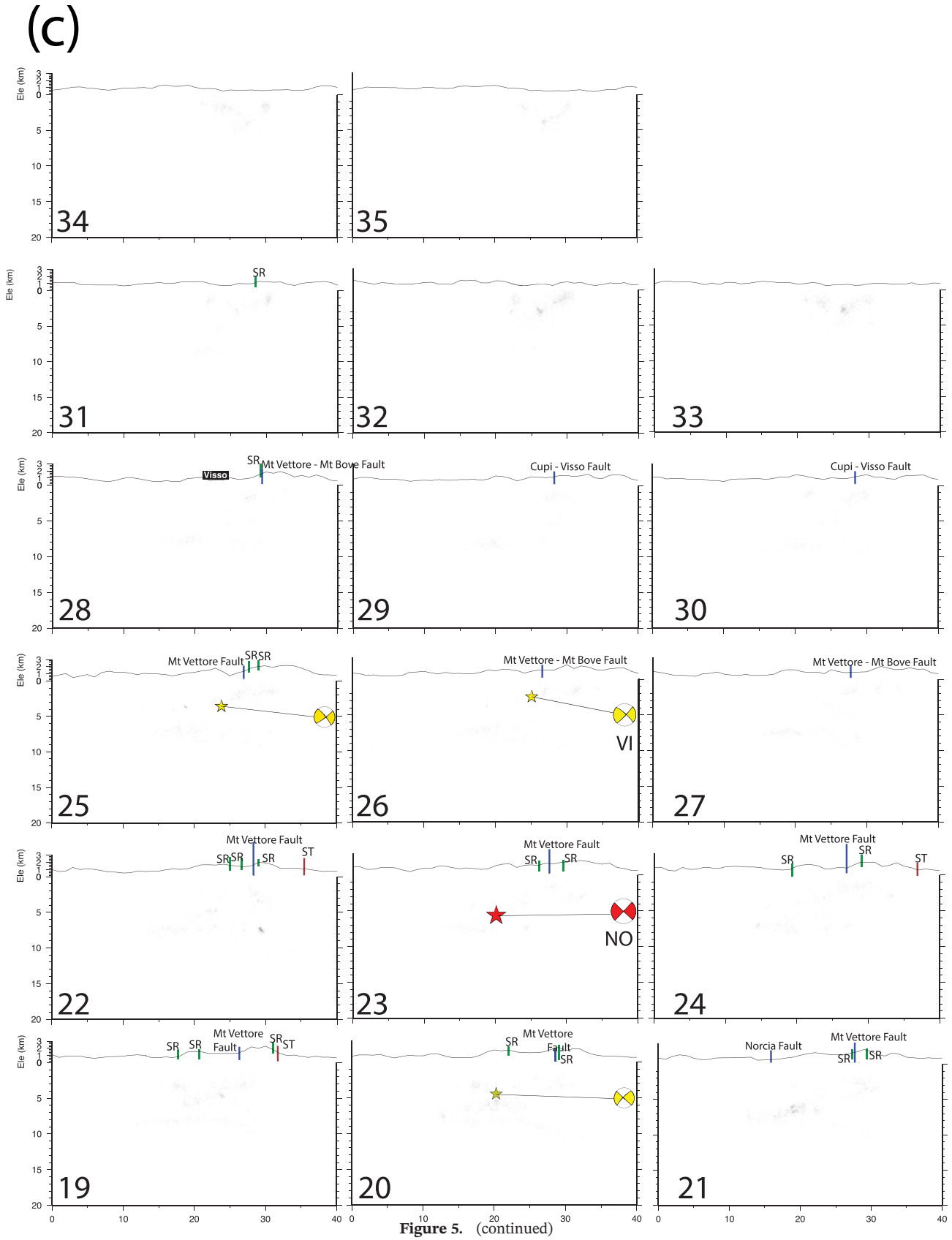

Figure 5. (continued)

In sections 7–9, the distribution with depth of the aftershocks of the four $5.0 \leq M_W \leq 5.5$ Campotosto events is aligned along a roughly kinked fault geometry whose direct connection to the Mt. Gorzano fault exposed at the surface is still not straightforward. While it is evident from the map view that the mapped Mt. Gorzano fault segment (see map in Figure 5a) completely bounds to the east the seismic activity, suggesting a spatial compatibility between the seismological and geological faults.

Minor synthetic and antithetic faults and small clusters of earthquakes are present in both the hanging-wall and foot-wall of the fault (for details, see light gray dashed lines Figure S2 in the supporting information).

3.3. Amatrice Earthquake

The transition from the Campotosto to the Amatrice area is marked in sections 9 and 10 (Figure 5b) by the appearance of the subhorizontal seismicity alignment at about 8–9 km depth already identified in Chiaraluce, Di Stefano, et al. (2017) and interpreted as an active shear-zone by Vuan et al. (2017). This shear zone appears to cut off the seismicity related to the normal faults at a depth of about 8 km.

Sections 10 to 14 (Figure 5b) cut through the M_W 6.0 AM rupture zone south of the AM epicenter (red star in section 13) and the Sibillini Thrust. These sections do not show a SW dipping plane because of lack of aftershocks within the rupture area. The geometry emerges again when faults are activated that cross the Sibillini Thrust front (sections 14–20; Figures 5b and 5c).

The Sibillini Thrust cuts through the coseismic slip surface of the Amatrice earthquake between Mt. Gorzano and Mt. Vettore (Chiaraluce, Di Stefano, et al., 2017; Tinti et al., 2016). The mainshock caused

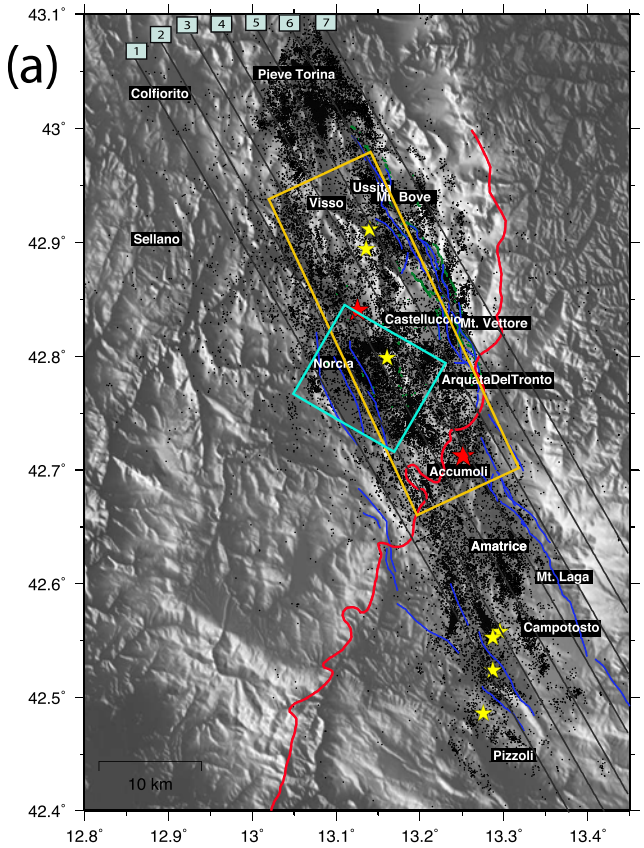

Figure 6. (a) Map view of the relocated aftershocks with slip areas superimposed. Legend is the same as Figure 5(a). The orange box is the surface projections of the Norcia M_W 6.5 slip area for the main fault, and the cyan box is the Norcia M_W 6.5 slip area for the secondary fault (Scognamiglio et al., 2018). Dark gray annotated lines are locations of along strike profiles shown in (b). (b) Cross sections along the N150E-oriented profiles shown in (a). Black dots are the AVN aftershocks, yellow stars are the $5.0 \leq M_W < 6.0$ earthquakes, red stars are the $M_W \geq 6.0$ earthquakes. The red ticks at surface denote the ST trace, and the green ticks the surface ruptures (Pucci et al., 2017).

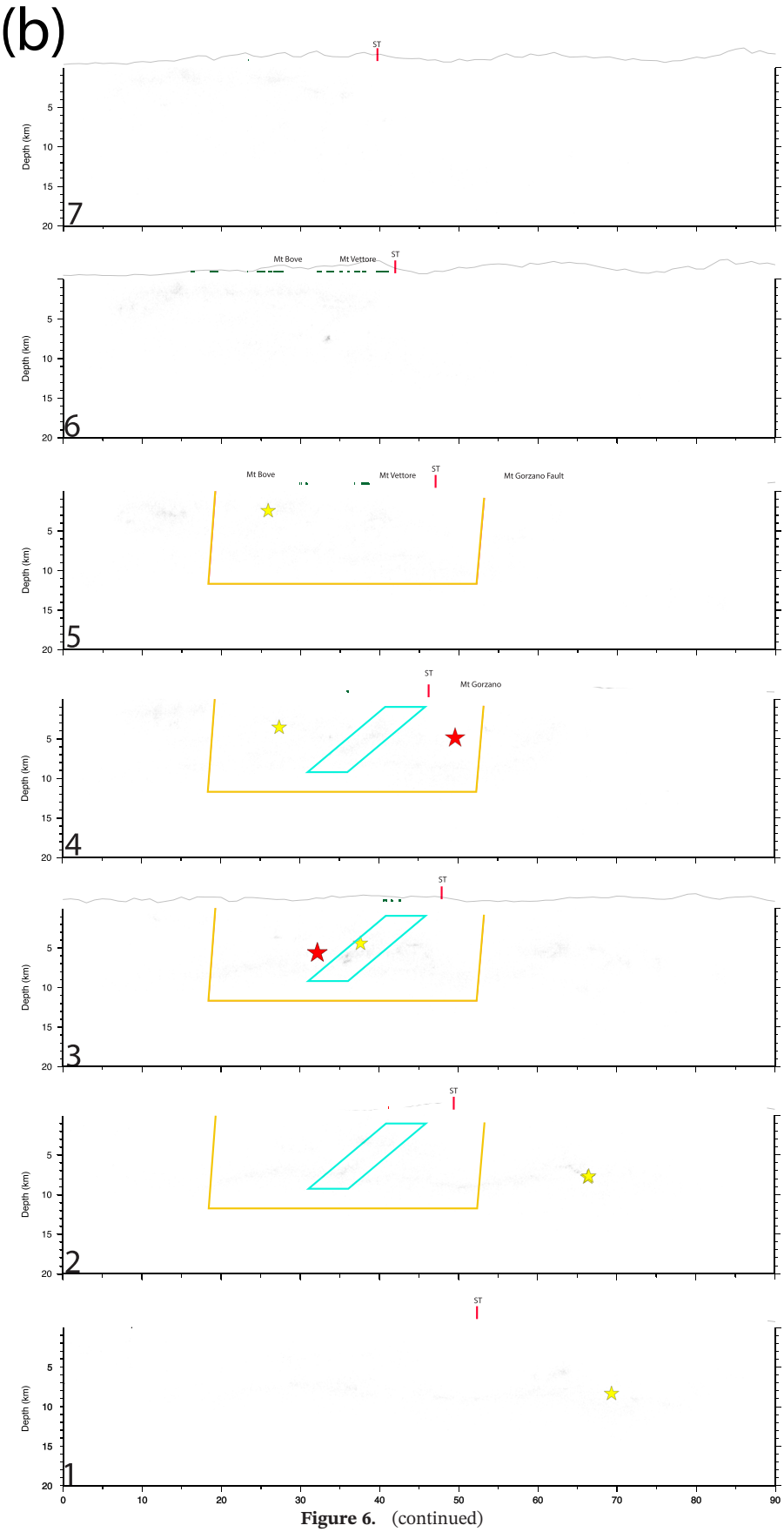

Figure 6. (continued)

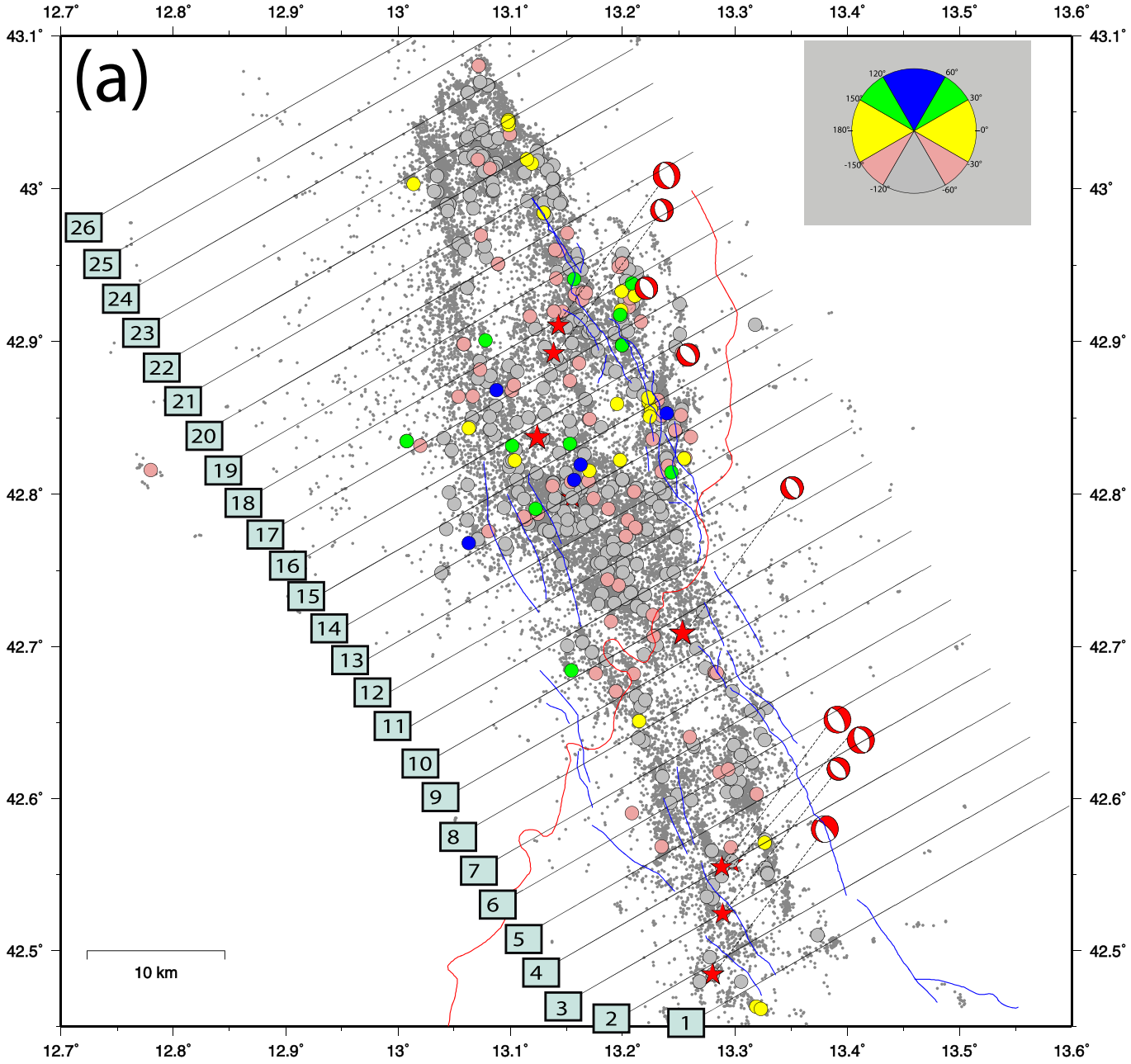

Figure 7. (a) Map of the aftershocks focal mechanism solutions color coded by kinematics as described by the top-right inset. The inset associates colors with ranges of rake angles. Light gray circles are for normal solutions, pink circles are for trans-tensional solutions, yellow circles are for strike-slip solutions, green circles are for trans-pressional solutions, and blue circles are for thrust solutions. Dark gray lines are the sections reported in (b). (b) Cross section along profiles shown in (a). Cross sections have the same orientation as in Figure 5 but include events within +/−1.5 km from each profile. Aftershock focal mechanisms distribution along the vertical sections, oriented orthogonal to the strike (150°) direction and centered on the M_W 6.5 Norcia earthquake. Orange beach balls represent focal mechanisms with dip angles lower than 30°. In both (a) and (b), gray dots are the AVN aftershocks, the red stars are Mw > = 6.0, the yellow stars are 5.0 < = Mw < 6.0, the red line and ticks are the trace at surface of the ST, the blue lines and ticks are the normal faults.

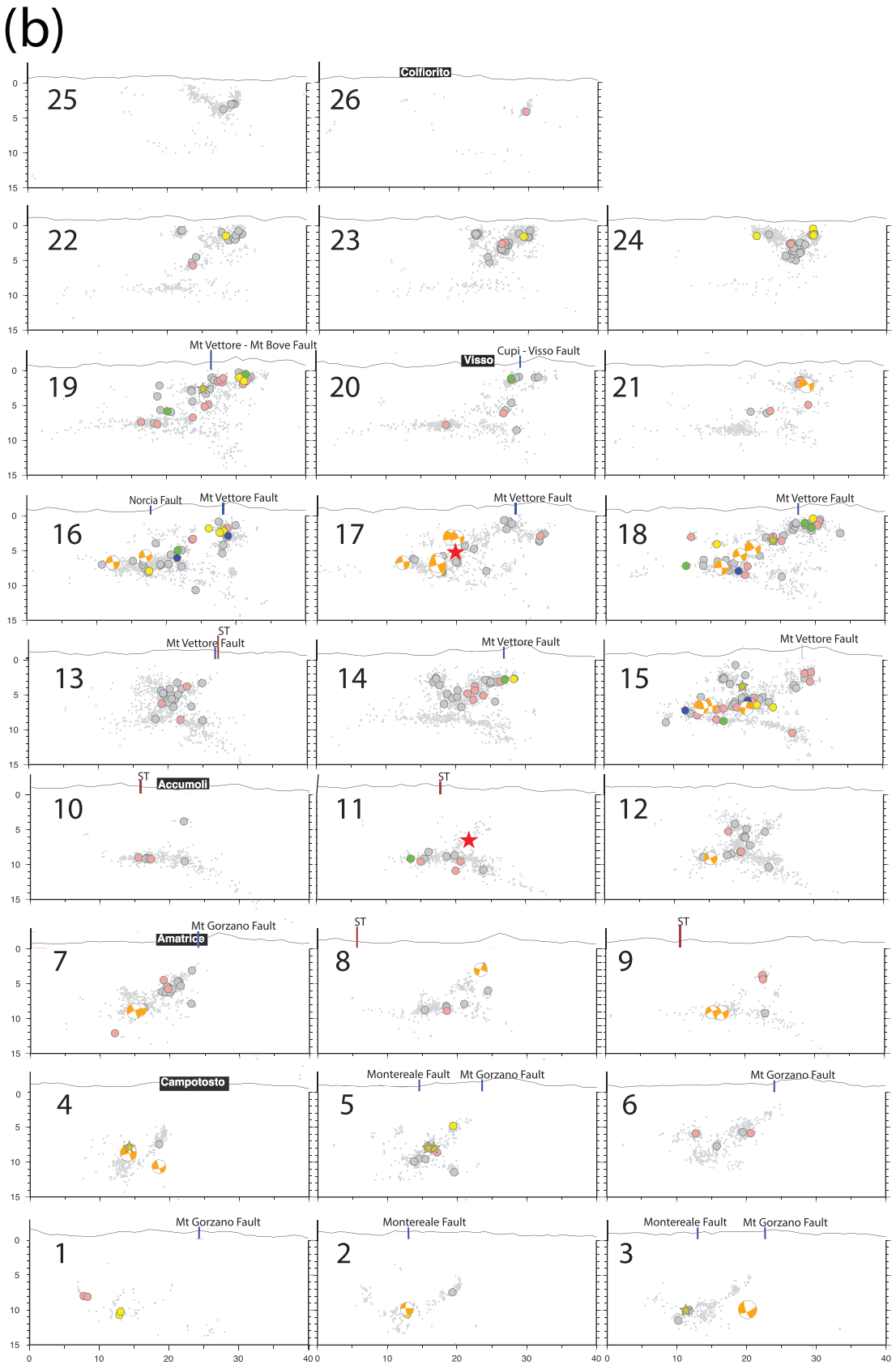

Figure 7. (continued)

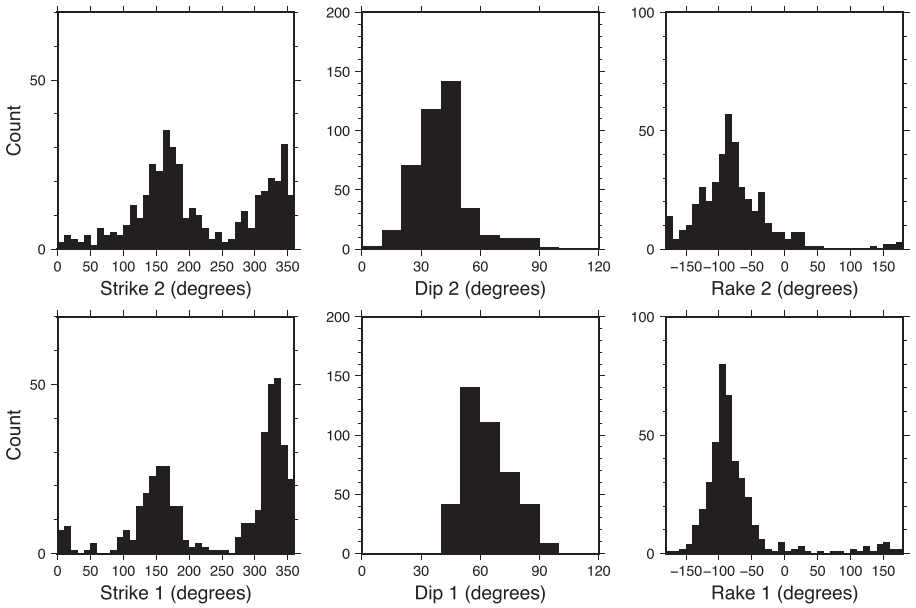

Figure 8. Histograms showing strike, dip, and rake distribution of the two fault planes of the focal mechanisms reported in Figure 7.

the first set of coseismic surface ruptures on Mt Vettore while early aftershocks occurred on both the northern segment of the main fault (Mt. Vettore-Mt. Bove Fault system) and on the antithetic fault that hosted the strongest aftershock (M_W 5.4, section 20).

From section 10 to 14, the seismicity is progressively more clearly confined at depth along the subhorizontal SZ. The structure extends to the north-east reaching 15–16 km depth (sections 13,14) showing a low east-dipping trend of ~20°.

In sections 11–13, the shear zone is more clearly defined than in other sections but still shows the same dip. The Amatrice mainshock (section 13 of Figure S2) locates at about 5 km of depth (see Table 2), shallower than the location by Chiaraluce, Di Stefano, et al. (2017) catalog (~8 km). However, the 5 km depth is consistent with the active fault which emerges in section 16 and north of it, where we observe the intersection between the main AM fault plane and its antithetic structure that was activated, 1 hr later, by a M_W 5.4 aftershock (yellow star in section 20 of Figure 5c). Earthquakes are sharply aligned well imaging the

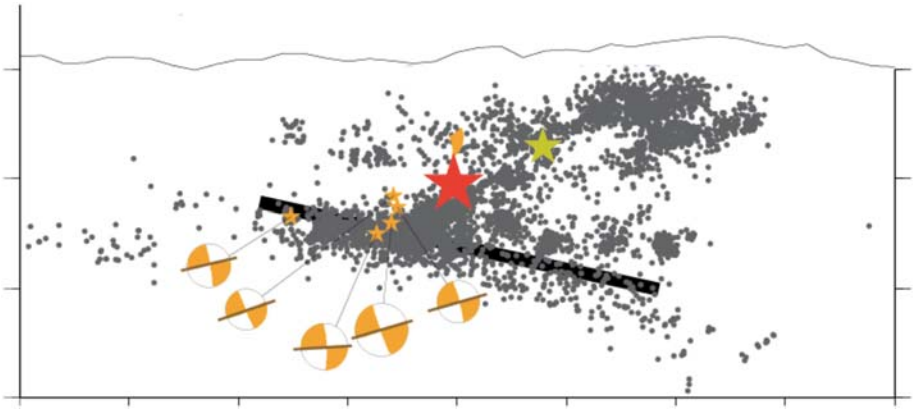

Figure 9. From Figure 7b, superposition of seismicity included in sections 16, 17, and 18. Red star is the NO position while yellow star is the VI position. Orange stars are the events with MW ≥ 3.5 having a dip angle less than 30°. Beach balls report the associated focal mechanisms.

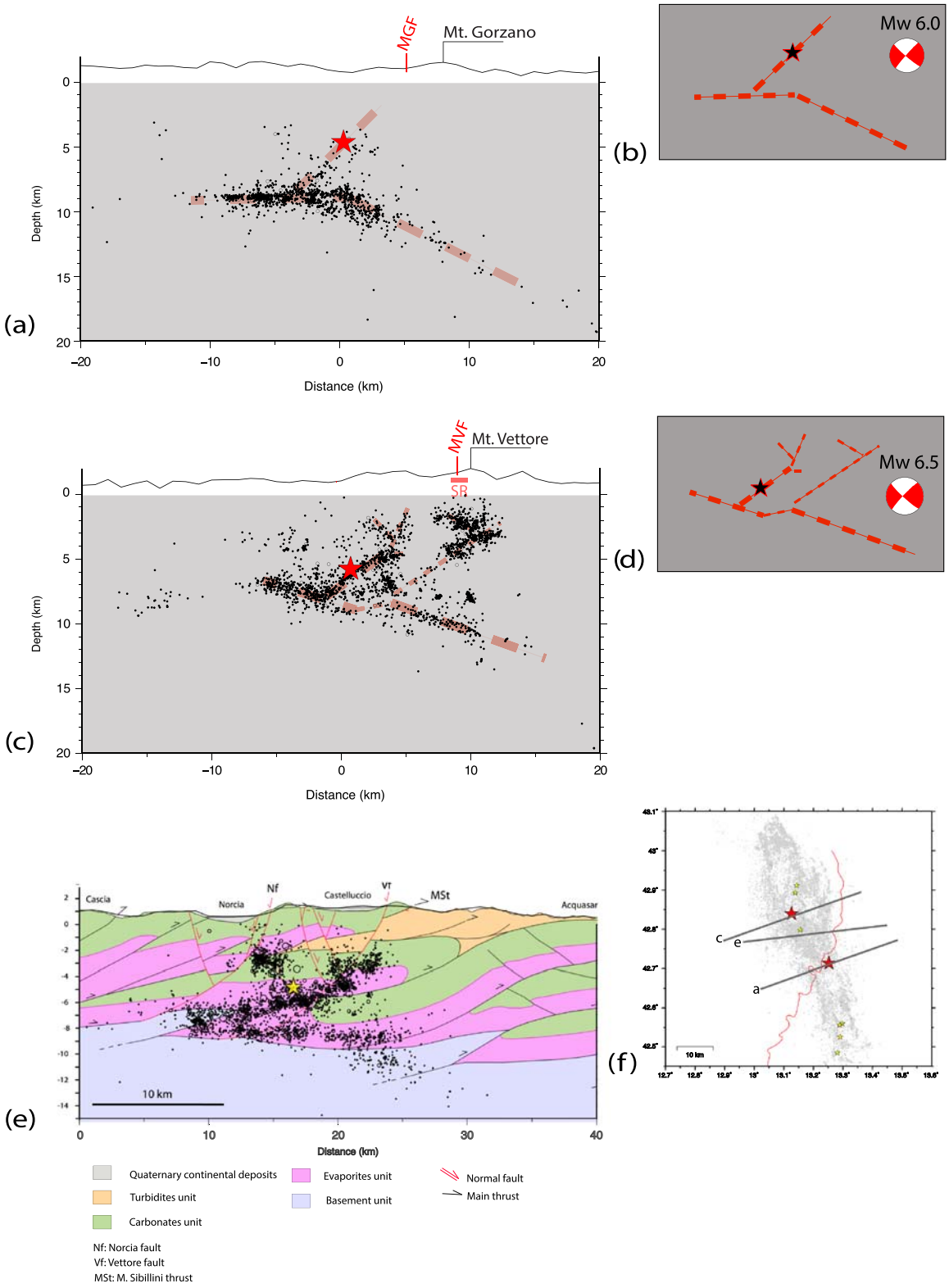

Figure 10. (a) Vertical section centered on the AM; (b) simplified sketch of the SZ and main fault along (a) section; (c) vertical section centered on the NO; (d) simplified sketch of the SZ, the main fault and syn- and antithetic minor faults along (c) section; (e) projection of the aftershocks and of the M_W 5.4 (24 August 2016; yellow star) along section S1 of Porreca et al., (2018) with relative lithologies; (f) map showing the traces of a, c, and e sections. The width of all the vertical sections is +/− 2 km, while the orientation is N70°E for (a) and (c) and ~N80°E for (e). The black circles are the aftershocks of AVN and are scaled with the magnitude.

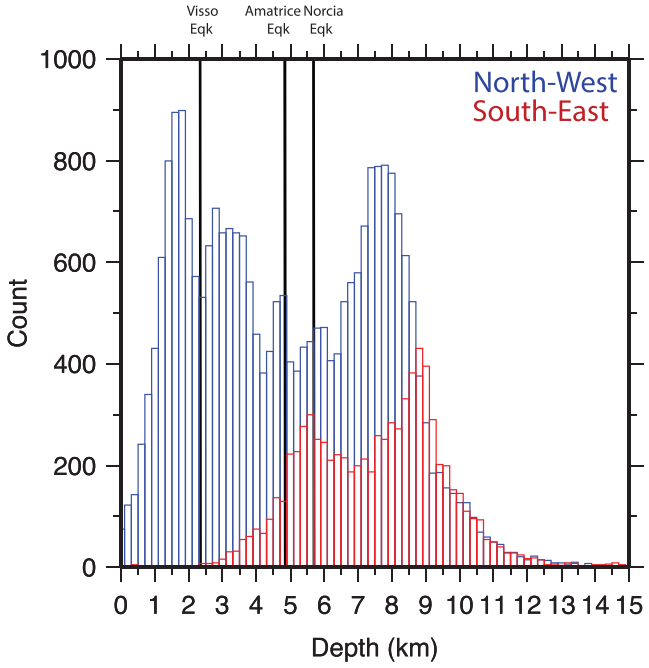

Figure 11. Histograms showing the number of events vs depth, south-east of ST (red bars), and north-west of ST (blue bars). Black lines indicate the depths where the strongest events ($M_W \geq 5.9$) of the sequence nucleated.

subhorizontal structure at about 8–9 km depth, the SW dipping main fault plane, and the antithetic faults. Section 18 shows particularly clear pattern of the synthetic, antithetic, and subhorizontal structures.

3.4. Norcia Earthquake

Seismicity distribution from section 19 to 24 (Figure 5c) maps the fault system activated by the M_W 6.5 Norcia earthquake on 30 October 2016, the strongest shock of the whole sequence. As shown by the space-time diagram and documented by the surface ruptures mapped soon after the AM earthquake (Pucci et al., 2017), this area was previously active. The Norcia earthquake, nucleating a few kilometers NW of the town of Norcia, reruptured the Mt. Vettore on the same fault plane as the Amatrice event did, strongly increasing the throw measured on the surface ruptures and extending them to the NW toward Mt. Bove. Our locations indicate that this sector is characterized by a very complex interaction between synthetic and antithetic fault planes in both the hanging wall and the footwall of the main fault and between the fault system and the SZ.

From section 19 northward, the geometry described by the seismicity starts to change: The subhorizontal SZ, which up to here marked the termination of the main fault at depth, starts separating from overlying faults by at least ~1 km. It also hosts a larger number of earthquakes compared to the Amatrice sector, and its width is estimated to be about 1 km. The east-ward dip of about 20° is almost constant. The normal fault geometry seems to be more complicated, as it starts to bend toward the surface where it gets closer to the outcrop of the shallow low angle (~27°) thrust faults. From section 22 northward, the main normal fault plane is subdivided into two parallel structures (see Figure S3, sections 22 and 23). Section 23 includes the M_W 6.5 hypocenter, placed at about 5.8 km. This hypocenter is 1.5 km shallower than the location by Chiaraluce, Di Stefano, et al. (2017; see Table 2), and therefore puts the nucleation point on the deeper portion of the fault plane, above the intersection between the normal fault and the shear zone. Finally, section 24 marks the transition to the Visso area.

3.5. Visso Earthquake

Moving along strike from section 25 to section 29 (Figure 5c), we show the alignment of seismicity along the Visso fault plane, indicating a dip of about 60°SW. Section 26 includes the M_W 5.9 Visso mainshock (26 October 2016), and section 25 includes the M_W 5.4 foreshock preceding the mainshock by 2 hr. Both hypocenters are shallow (2.5 km and 3.5 km, respectively) and are consistently placed at the bottom of the identified fault segment in agreement with the mainshock's computed slip distribution (Chiaraluce, Di Stefano, et al., 2017).

The subhorizontal SZ in the area is still present at about 8 km of depth, though the alignment is less sharp here. In the foot-wall of the Visso fault plane, several minor subparallel structures are imaged by earthquakes alignments. In section 29, the Visso fault plane is lost while the deep subhorizontal shear-zone is still active.

The northern edge of the Visso fault system undergoes yet another change in the geometry activated faults, while SZ seismicity peters out (sections 30 and 31).

The region further north experienced strong aftershock activity that lasted for many months, including the occurrence of several earthquakes with M_W up to 4.7 (sections 32 to 35). The seismicity indicates a small, shallow (above 5 km depth) synthetic/antithetic fault system. The SZ is almost completely absent here confirming its aseismic behavior observed during the 1997 Colfiorito sequence (Chiaraluce et al., 2003).

3.6. Longitudinal Sections

In order to characterize the along strike fault system geometry, with special focus on the subhorizontal shear zone and its relationship to the overlaying normal fault, we produced a set of longitudinal cross sections (see

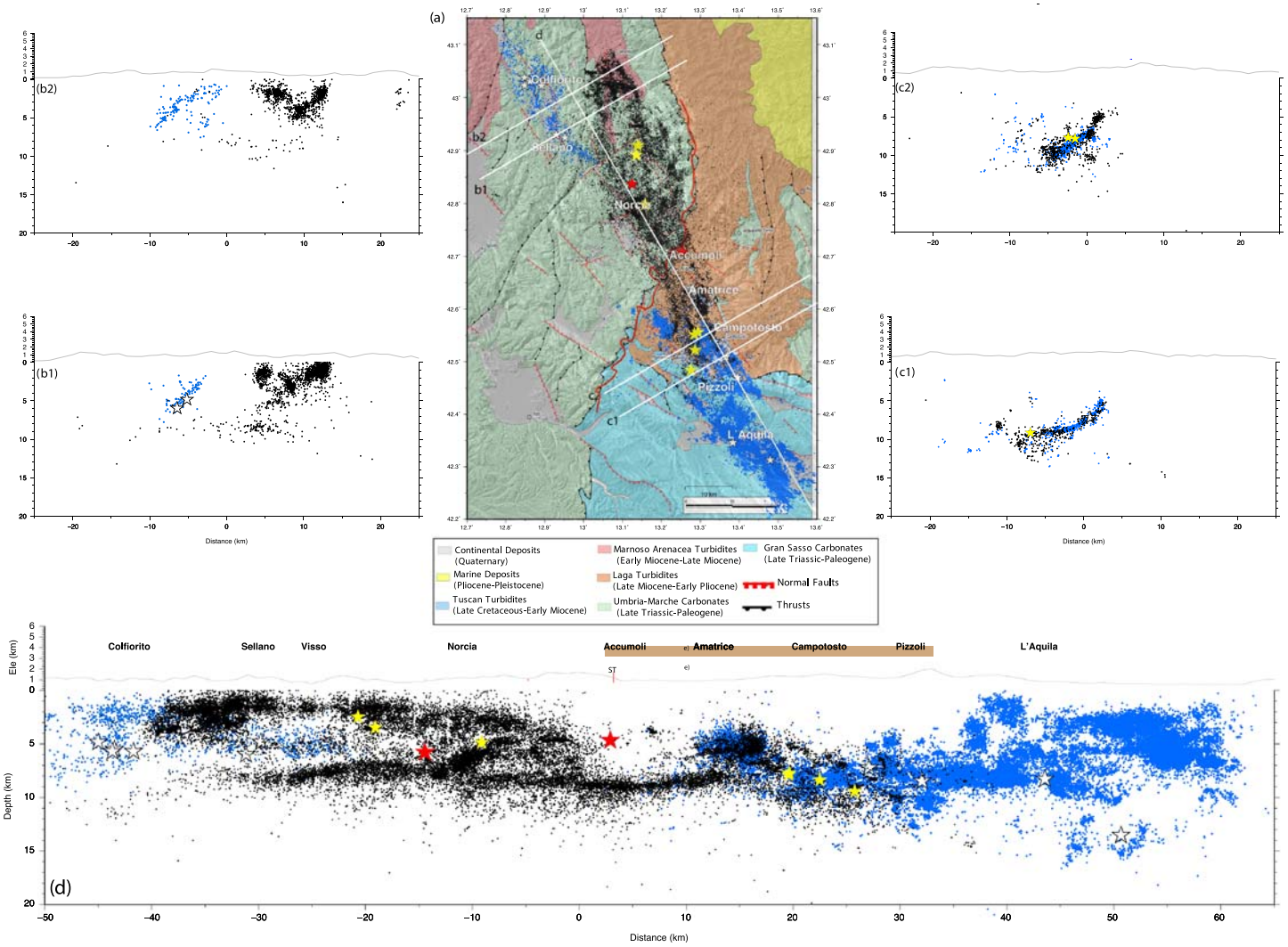

Figure 12. (a) Map view of the relocated aftershocks (black dots) superposed on the geological map, modified after Porreca et al. (2018). Yellow stars are the $5.0 \leq M_W < 6.0$ earthquakes, red stars are the $M_W \geq 6.0$ earthquakes, light blue dots are the Colfiorito 1997 (north-west) and the L'Aquila 2009 (south-east) seismic sequences. Red lines are the traces of ST, the green lines are the surface ruptures (Pucci et al., 2017), and the white lines are the traces of the vertical sections. The orientation and width are N60°E and +/−1.5 km, respectively, for sections b and c, and N150°E and +/−2.5 km for section d.

Figure 6a, dark gray lines, for location). Each section (Figure 6b) includes events located within +/−1.5 km of distance from the vertical plane. Moving from southwest (section 1) toward northeast, the geometry of the SZ shows a clear along strike lateral continuity even when crossing the Sibillini thrust: It stretches over 60 km in sections 1 to 3, and the band of seismicity is generally around 2 km thick. Our images show that while the SZ is clearly subhorizontal, local variability of the longitudinal dip can be observed (Chiaraluce, Di Stefano, et al., 2017; Vuan et al., 2017), with a wavy shape with a wavelength of about 30 km and increasing north of VI and south of AM. Segmentation of the SZ is indicated in section 2 and section 3, in places where the high angle normal faults root, and where the northern portion of the system seems to over-thrust the southern one.

In section 3, which includes the M_W 6.5 Norcia hypocenter (at ~6 km of depth), as well as in the nearby sections 2 and 4, the earthquake distribution is quite complex, possibly due to the activation of oblique and trans-tensional faults associated to the M_W 6.5 rupture process (Cheloni et al., 2017; Scognamiglio et al., 2018). These authors suggest the contemporaneous and thus coseismic activation of the Mt. Bove-Mt. Vettore normal and the ST oblique lateral ramp faults during the M_W 6.5 NO event. In order to

identify the ramp activation signature through the analysis of the aftershocks distribution, we draw in the longitudinal sections (2, 3, and 4) the projection of the (cyan) box as modeled by Scognamiglio et al., (2018). The earthquake alignment contained within the box is possibly coherent with the proposed geometry.

Section 4 contains the M_W 6.0 hypocenter location at ~5 km of depth and shows the coherent lack of seismicity past the perimeter of the mainshock slip distribution (Hartzell & Heaton, 1986), suggesting complete stress drop during the main rupture. The SZ is still present NW of the ST (0–35 km distance) though it slowly fades, while it is almost absent SE of ST especially from section 5 on.

Similarly, the seismicity related to the normal fault system, above the SZ, is mainly concentrated northwest of the ST and disappears 10–15 km south-east of the M_W 6.5. The seismicity distribution in sections 5, 6, and 7 suggests not only the interference between the inherited compressional structures (e.g., ST) and the emplacement of the extensional system (e.g., Mt. Vettore and Mt. Bove) but also the change in the mechanical properties of the lithologies embedding the two fault system portions.

Section 5 contains the M_W 5.9 VI hypocenter location, the yellow star at 2.6 km of depth. It is worth noting that both probabilistic absolute locations with stations corrections and the DD locations of the earthquakes with $M_W \geq 5.0$, with the exception of the M_W 6.0 and 6.5, show an inverse trend between latitude and depth, with depth shallower in the northern region. This aspect will be approached in the section 5.

4. Kinematics of the System

We merged all the available focal mechanisms from waveforms inversion for the events with $M_W > 3.0$ from INGV TDMT (web-service: http://cnt.rm.ingv.it/tdmt; Scognamiglio et al., 2009) and the Moment Tensor Solutions for Italy (by Malagnini at http://www.eas.slu.edu/eqc/eqc_mt/MECH.IT; Herrmann et al., 2011). Aftershock focal mechanisms are shown in map view and in cross sections (respectively in Figures 7a and 7b); solutions are color coded by type of mechanism: normal (gray), trans-tensional (pink), strike-slip (yellow), trans-pressive (green), and thrust solutions (blue).

Normal and trans-tensional mechanisms coherently characterize the main fault planes and their antithetic planes. Dip from focal mechanisms is consistent with the dip retrieved from the seismicity distribution. The majority of aftershocks show extensional kinematics: 70% exhibit normal fault mechanisms, and 20% are trans-tensional. Other mechanisms include strike-slip (7%), trans-pressive (2.6%), and only less than 1% are thrust faulting. These results are quite consistent with the NW-SE normal faulting style observed for the mainshocks. As shown in Figure 8, the majority of the strikes align around 150° or 330° both on the fault and auxiliary planes; The same is for the rake distribution that in both of the planes result in a majority of ~−90° while the medians of dip distribution are different between plane 1 (~55°) and plane 2 (~ 45°).

A more complex and heterogeneous pattern is found for solutions of shallow events (depth 0–2 km) occurring at the tip of the Norcia normal fault at its footwall (sections 19–20 and 16–18). In order to better characterize the kinematic of the basal SZ, we reported (in orange) the focal mechanisms which show one low angle plane, dip less than 30°, between the two nodal ones. The majority of these events, whose beach ball size reflects the event magnitude, nucleated close the SZ, together with a set of strike slip events and some (very few) thrusts (see sections 12 and from 15 to 18). It is important to note that the focal mechanisms solution showing a low angle plane, located nearby the SZ, are not geometrically coherent with the dip geometry of the structure imaged by seismicity distribution. The dip direction of the low angle planes lying along the SZ is in fact generally SW-trending, thus dipping in the opposite direction from the dip shown by aftershocks distribution (see Figure 9). This agrees with the hypothesis proposed by Chiaraluce, Di Stefano, et al. (2017) suggesting that these events may rupture the higher angle planes as a brittle response of the subhorizontal structure to a deeper and possibly a seismic deformation process. The other possibility is that these events are not placed within the SZ but instead nucleate along here SW-dipping planes where they sole into the SZ. While the events with a low angle plane located at shallower depths (e.g., along the higher angle structures) are both kinematically and geometrically consistent (see cross sections 8 and 18).

5. Discussion and Conclusions

As documented in both historical and instrumental recordings, the AVN seismic sequence is typical for the seismic behavior of that part of the Apennines mountain belt to the extent that the fault system is activated by a series of shallow ≈ M_W 6.0 mainshocks that occurred within periods of a few days, weeks, or months. The active faults include SW-dipping normal fault segments striking along the axis of the Central Apennines and several associated minor syn- and antithetic fault splays.

We used double-difference locations of 34 k aftershocks with $M_L \geq$ 1.5 recorded up to 18 January 2018 in order to analyze their distribution in space and time, together with the kinematic of the larger events ($M_W > 3$). The early aftershocks of the first mainshock (24 August 2016; AM Mw 6.0) spread almost bilaterally (Figures 4a and 4b) starting from the Accumoli village, coherently with the bilateral rupture directivity proposed by Tinti et al. (2016) and Calderoni et al. (2017). On 26 October, the M_W 5.9 VI earthquake occurred to the north with a strong unilateral rupture directivity, in agreement with its early aftershocks migrating toward NW. On 30 October 2016, the M_W 6.5 NO earthquake nucleated only 5 km to the south of VI and propagated bilaterally for about 40 km. On the 18 January, four $5.0 \leq M_W \leq 5.5$ earthquakes hit the Campotosto area preceded by a small cluster of seismicity in December. As this preshocks activity is present both in the shear zone and above it, probably here the fault tip coincides with the SZ.

The space-time diagrams show differences between the two diverse upper crustal lithologies embedding the activated fault segments. The portion below Norcia (from −5 to −20 km in Figure 4a), hosting the northern slip patch of the AM (from Tinti et al., 2016), is embedded in the Umbria-Marche domain, composed by Upper Triassic-Miocene carbonate platform and slope-basin succession and produces a higher number of aftershocks with respect to the southern one, placed below Amatrice (from 0 to 10 km in Figure 4a) that is set within the Laga Foredeep domain consisting of Upper Miocene Flysch deposits. Such diversity is not reflected in the seismicity distributed along the basal shear zone suggesting the presence of a similar lithology.

It is still under discussion to what extent, if at all, the Sibillini thrust is controlling the extensional deformation in the overlying crust and potentially hosting coseismic slip during the M_W 6.5 event (Tinti et al., 2016; Chiaraluce, Di Stefano, et al., 2017, Pizzi et al., 2017; Cheloni, Falcucci, et al., 2019) as a secondary fault. This latter case would imply the reactivation in terms of kinematic inversion, of the preexisting ST oblique ramp, formed during the late Pliocene compressive phase (Bonini et al., 2019; Buttinelli et al., 2018; Chiarabba et al., 2018) as originally proposed by Scognamiglio et al. (2018). This model is partially corroborated by the earthquakes alignments we highlighted in Figure 6 (see earthquakes clustered within the cyan box). The coseismic reactivation of compressional structures that is not oriented in direction of the present regional stress field has a strong impact on the hazard estimate; it might be an undervaluation of the seismic hazard considering such inherited faults as permanent barriers segmenting and limiting the length of the active faults (e.g., no implications for maximum magnitude). While regarding the maximum extent to the south of the source responsible for the NO event after rupturing along the northern Mt. Vettore-MT. Bove segment when possibly propagating along an oblique portion of the Sibillini thrust (as proposed by Scognamiglio et al., 2018), we state that our reconstruction in space and time, and focal mechanisms, is consistent with a composite rupture model previously proposed for the M_W 6.5 Norcia earthquake, where the mainshock ruptured along the northern Mt. Vettore-MT. Bove segment and then possibly propagated along an oblique portion of the Sibillini thrust. At the same time, we are aware that our data are not definitive because, as for the AM mainshock, we miss the early aftershocks.

To better highlight the geometry of the two main fault segments, we show in Figure 10 two comprehensive cross-sections centered on the AM M_W 6.0 (Figure 10a) and NO M_W 6.5 (Figure 10b) mainshocks, where we projected 4 km (+/− 2 km) of seismicity. In order to optimize earthquakes clustering, ideally occurring along the main fault, we performed a search for the best cross section strike, with 5° steps. The chosen orientation reported in Figures 10a and 10b is N70°E, thus slightly different from the N60°E orientation used in Figure 5, based on the mainshocks focal mechanism solutions. According to these optimally oriented sections, we observe the dip angles of the two faults being 48° and 42° for Amatrice M_W 6.0 and Norcia M_W 6.5, respectively. Including more aftershocks along the AM section allows a slightly better imaging of the fault plane, pointing to the Mt. Gorzano fault outcrop mapped at the surface (MGF in Figure 10a; northern portion of the

Mt. della Laga system). The same alignment with the structures mapped at the surface is visible in Figure 10b where we observe that the M_W 6.5 fault plane imaged by the earthquakes distribution matches perfectly with the coseismic surface ruptures mapped along the Mt. Vettore fault trace (MVF; from Pucci et al., 2017; Villani et al., 2018).

However, comparing our mainshocks' relative locations with the absolute ones (Table 2), we observe that they are now located along the deeper portion of the normal fault planes but not at their tip intersecting the SZ, as previously reported by Chiaraluce et al., 2017 in their preliminary analysis. This indication is also different from what Chiaraluce (2012) and Valoroso et al. (2013) observed for the 2009 L'Aquila M_W 6.1 mainshock. Another difference between the anatomy of these two faults (2009 and 2016) is the fault zone width; the most recently activated segments show in fact thicker fault zones. This can be due to both the earthquakes location resolution and the intrinsic mechanical conditions of the faults mainly related to the fault age and hosting lithology. Further analysis is needed to unravel this important aspect; in the meantime, we can contribute in the discussion by trying to correlate the seismic activity with the lithology and subsurface geology by projecting (in Figure 10c) the relocated seismicity along the available structural section derived from seismic reflection profile data migrated at depth and interpreted, by Porreca et al. (2018). The section crosses the Mt. Vettore structure hosting the northern patch of the M_W 6.0 AM earthquake. The cross section has a ~N80°E strike; thus, earthquake alignment shows an apparent (e.g., lower) dip. Despite that, it is quite clear the interference between the inherited compressional structure and the younger extensional ones. Moreover, it is confirmed that seismicity is confined within sedimentary succession, as already proposed by Chiaraluce, Barchi, et al. (2017) from the analysis of background and 1997 and 2009 seismic sequences activity. The along strike wavy basal SZ (see longitudinal cross sections in Figure 6b) seems here clearly related and influenced by the depth of the basement.

The analysis of these cross sections allows us to confirm the strongly complex geometry of the whole system composed by relatively younger normal faults emplaced in an environment modeled by the previous compressional tectonics. Additional evidences of the seismicity compartmentalization within specific layers can be deduced from the hypocenter's distribution at depth. In Figure 11, we represent the frequency classes of the locations' depth, grouping earthquakes by two macro-areas, North-West and South-East of the ST. The total amount of seismicity is much higher in the northern portion with respect to the southern one. In the NW volume, location depth distribution (blue histogram) shows two peaks, at 8 and 2 km of depth, with the shallower cluster containing a very large number of events (depth less than 4 km) related to the activation of both minor fault splays (e.g., of the ST thrust) and the shallow portion of the main fault planes. The southern volume too (red histogram in Figure 11) shows two distinct peaks. One shallow around 5 km and a deeper one, around 8 km depth, related to the so called SZ. The main difference between the two seismogenic zones here is the general lack of shallow seismicity (<5 km) in the southernmost area.

We consider the depth distribution and the geometry of the SZ structure, together with seismicity distribution of the close Colfiorito 1997 and L'Aquila 2009 sequences, as key elements to discuss and interpret the activation and the geometry of this continuous fault system. To this end, we plot together in Figure 12 the aftershocks from three catalogues whose hypocenters locations have been computed with the same technique (HypoDD; Waldhauser & Ellsworth, 2000) including waveforms similarity measurements (Chiaraluce et al., 2003 for 1997 Colfiorito; Valoroso et al., 2013 for L'Aquila 2009 and this study for AVN2016-17).

A general introductory observation is that this 120 km long system, composed by 10–30 km long normal fault segments activated by cascades of $5.5 < M_W < 6.5$ events occurring within days-weeks-months, was activated only within 20 years. While the historical (Chiaraluce, 2012; Rovida et al., 2019) and paleo-seismological (Galadini & Galli, 2000; Galli et al., 2019) data suggest that their previous activation spanned between hundreds and thousands of years, posing strong suggestions to time-dependent hazard approaches.

About the structural style, we observe that all the segments terminate around 10 km of depth even if with different modalities. The whole Colfiorito system to the north (from −20 to −50 km in Figure 12d) as well the southern portion of the L'Aquila one (from 40 to 8 km in Figure 12d) do not show a clear basal zone of seismicity (e.g., SZ) bounding at depth the high angle normal faults. While for the 1997 sequence, this may be due to the completeness magnitude resolution; this is not the case for the 2009 one. Below Amatrice and Norcia areas, we map a distinct SZ with an almost horizontal geometry. The high angle

normal faults, where the largest events nucleate, are placed on top of it. However, it is interesting to note that the mainshocks nucleation points (hypocenters) are located in the deeper portion of the faults, but they are placed relatively far from their intersection with the shear zone. In addition to this, an aseismic gap exists between the deepest part of the normal fault; see below the Mt. Vettore and the Visso earthquake regions. This may be due to heterogeneous distribution of frictional properties along the faults, further complicating the interpretation of the mechanisms driving strain partitioning in this region. Conversely, in the Campotosto area, we do not see a proper SZ. Instead, the faults hosting the largest events go flat with depth (section C1 in Figure 12). It seems that where we observe the existence of higher angle planar normal faults (like L'Aquila and Colfiorito segments), the deformation can avoid such decollement. While where we have more complex, possibly younger, extensional structures, interfering with or tectonically inverting inherited compressional structures, a basal and almost flat layer, becomes structurally functional.

Another interesting aspect regards the shallow areas placed along the strike of the system missing aftershocks. Looking at the longitudinal section (Figure 12d), we see that the area surrounding the AM hypocenter, that slipped coseismically during the mainshock, does not host aftershocks above 7 and 8 km of depth. The same occurs in the area placed to the south, below Campotosto and Pizzoli, between 0 and 5 km of depth. However, by adding all the coseismic displacements generated by all the events with magnitude larger than 5 occurred in the area from 2009 along the Campotosto sector, Cheloni, D'Agostino, et al. (2019) have shown that this shallow sector is also missing coseismic slip. All these observations together pose both a mechanical and a hazard issue to be addressed. Our explanation for such a behavior is related to the local geology. By overlapping the geological and the seismicity map, we observe in fact that the shallow area missing aftershocks is occupied by the Laga formation outcropping at the surface, made of turbidites of siliciclastic deposits. The exact information about the depth distribution of this lithology is missing, but at least we know that it goes from 1 to 4 km of depth all along the Accumoli-Pizzoli alignment. Our idea is that this lithology, like other velocity strengthening materials, can become unable due to rapid shear (e.g., hit by a fast wave front; Noda & Lapusta, 2013). While they may respond only with aseismic deformation (e.g., stable creeping) when locally stressed. This is a key aspect deserving further investigation.

The AVN system terminations also present worth noting features. It is clear, in fact, that this sequence fills a gap between the northern 1997 Colfiorito (M6) earthquake and the southern 2009 L'Aquila (M6.1) and that it reactivated, in a series of $M_W \geq 5.0$ events, part of the Campotosto fault previously ruptured during L'Aquila. In Figure 12, sections b1 and b2, we observe that the main 1997 and 2016–17 faults lie parallel to each other. While to the south (sections c1 and c2), the AVN seismicity in the Campotosto area along the Mt. della Laga occurred on the same structure activated during 2009, continuing it along strike and elongating it toward the surface, up to 4 km depth. This suggests that stress was released that has either build up or not completely released since the L'Aquila event.

A final assertion regards the resolution of the earthquake catalog we generated for the AVN sequence that we consider an important evidence of the positive evolution of the Italian monitoring system at regional scale. It is notable, in fact, that the data set (waveforms and *P* and *S* readings) we used to create this new catalog is routinely produced by the RSN National Seismic Network (INGV) in the 24/7 active seismic room with mainly monitoring aims. The consistency between this dataset and the high-resolution Colfiorito 1997 (Chiaraluce et al., 2003) and L'Aquila 2009 (Valoroso et al., 2013) ones, as shown in Figure 12 in terms of depths distribution and continuity of geometry, is remarkable. These are catalogs that have been retrieved with the same approach in terms of location procedure but starting from different pickings procedure as well as different seismic networks densities. This suggests that routine monitoring procedures at INGV can be augmented by implementing real-time double-difference methods (Waldhauser, 2009) which has the potential to improve our understanding of seismic sequences as they unfold.

Acknowledgments
We thank all the Institute of Geophysics and Volcanology (INGV) personnel on duty in the monitoring room and INGV Bulletin who generated the starting *P* and *S* onsets catalog. The earthquakes catalog is available on https://doi.org/10.5281/zenodo.3712731; arrival times observations, waveforms, and station information are available through ISIDe (Italian Seismological Instrumental and parametric Data-base; http://cnt.rm.ingv.it/iside) and related webservices. Waveforms are also accessible through the European Integrated Data Archive (EIDA) at http://eida.rm.ingv.it. Thanks to David Schaff for providing us with important suggestions and support in the cross-correlation processing. We would like to thank Massimiliano Barchi for furnishing us some geological information supporting our interpretations. We thank to anonymous reviewers for helpful suggestions and comments that imporved the manuscript. During this work, Maddalena Michele was supported by an Italian Civil Protection Grant (DPC-B2 cod. 0799040 and DPC-B2 cod. 0304.023) and Progetto PREMIALE (cod. 0551.020). Felix Waldhauser was funded by NSFGEO-NERC award 1759782.

References

Bonini, L., Basili, R., Burrato, P., Cannelli, V., Fracassi, U., Maesano, F. E., et al. (2019). Testing different tectonic models for the source of the Mw 6.5, 30 October 2016, Norcia earthquake (Central Italy): A youthful normal fault, or negative inversion of an old thrust? *Tectonics*, *38*(3), 990–1017. https://doi.org/10.1029/2018TC005185

Boschi, E., Pantosti, D., Slejko, D., Stucchi, M., & Valensise, G. (1990). Irpinia dieci anni dopo. *Special Issue, Annali di Geofisica*, *36*, 19–24.

Buttinelli, M., Pezzo, G., Valoroso, L., De Gori, P., & Chiarabba, C. (2018). Tectonics inversions, fault segmentation, and triggering mechanisms in the central Apennines normal fault system: Insights from high-resolution velocity models. *Tectonics*, *37*(11), 4135–4149.

Calamita, F., Pace, P., & Satolli, S. (2012). Coexistence of fault-propagation and fault-bend folding in curve-shaped foreland fold-and-thrust belts: Examples from the northern Apennines (Italy). *Terra Nova*, *24*(5), 396–406.

Calderoni, G., Herrero, A., & Di Alessandro, C. (2011). Combined Effect of Basin Resonance and Source Directivity: Implications for Long Period Hazard in the Apennines, Central Italy. Effects of Surface Geology on Seismic Motion.

Calderoni, G., Rovelli, A., & Di Giovambattista, R. (2017). Rupture directivity of the strongest 2016–2017 Central Italy earthquakes. *Journal of Geophysical Research: Solid Earth*, *122*, 9118–9131.

Carannante, S., Monachesi, G., Cattaneo, M., Amato, A., & Chiarabba, C. (2013). Deep structure and tectonics of the northern-central Apennines as seen by regional-scale tomography and 3-D located earthquakes. *Journal of Geophysical Research: Solid Earth*, *118*, 5391–5403.

Centamore, E., & Rossi, D. (2009). Neogene-quaternary tectonics and sedimentation in the central Apennines. *Bollettino della Societa Geologica Italiana*, *128*(1), 73–88.

Cheloni, D., D'Agostino, N., Scognamiglio, L., Tinti, E., Bignami, C., Avallone, A., et al. (2019). Heterogeneous behavior of the Campotosto Normal fault (Central Italy) imaged by InSAR GPS and strong-motion data: Insights from the 18 January 2017 events. *Remote Sensing*, *11*, 1482. https://doi.org/10.3390/rs11121482

Cheloni, D., De Novellis, V., Albano, M., Antonioli, A., Anzidei, M., Atzori, S., et al. (2017). Geodetic model of the 2016 Central Italy earthquake sequence inferred from InSAR and GPS data. *Geophysical Research Letters*, *44*, 6778–6787. https://doi.org/10.1002/2017GL073580

Cheloni, D., Falcucci, E., & Gori, S. (2019). Half-graben rupture geometry of the 30 October 2016 M_W 6.6 Mt. Vettore-Mt. Bove earthquake, central Italy. *Journal of Geophysical Research: Solid Earth*, *124*(4), 4091–4118. https://doi.org/10.1029/2018JB015851

Chiarabba, C., De Gori, P., Cattaneo, M., Spallarossa, D., & Segou, M. (2018). Faults geometry and the role of fluids in the 2016–2017 Central Italy seismic sequence. *Geophysical Research Letters*, *45*(14), 6963–6971.

Chiaraluce, L. (2012). Unravelling the complexity of Apenninic exten- sional fault systems: A review of the 2009 L'Aquila earthquake (central Apennines, Italy). *Journal of Structural Geology*, *42*, 2–18.

Chiaraluce, L., Amato, A., Cocco, M., Chiarabba, C., Selvaggi, G., Di Bona, M., et al. (2004). Complex normal faulting in the Apennines thrust-and-fold belt: The 1997 seismic sequence in Central Italy. *Bulletin of the Seismological Society of America*, *94*(1), 99–116.

Chiaraluce, L., Barchi, M., Collettini, C., Mirabella, F., & Pucci, S. (2005). Connecting seismically active normal faults with quaternary geological structures in a complex extensional environment: The Colfiorito 1997 case history (northern Apennines, Italy). *Tectonics*, *24*, TC1002. https://doi.org/10.1029/2004TC001627

Chiaraluce, L., Barchi, M. R., Carannante, S., Collettini, C., Mirabella, F., Pauselli, C., & Valoroso, L. (2017). The role of rheology, crustal structures and lithology in the seismicity distribution of the northern Apennines. *Tectonophysics*, *694*, 280–291.

Chiaraluce, L., Chiarabba, C., Collettini, C., Piccinini, D., & Cocco, M. (2007). Architecture and mechanics of an active low-angle normal fault: Alto Tiberina fault, northern Apennines, Italy. *Journal of Geophysical Research - Solid Earth*, *112*. https://doi.org/10.1029/2007JB005015

Chiaraluce, L., Di Stefano, R., Tinti, E., Scognamiglio, L., Michele, M., Casarotti, E., et al. (2017). The 2016 Central Italy seismic sequence: A first look at the mainshocks, aftershocks, and source models. *Seismological Research Letters*, *88*(3), 757–771. https://doi.org/10.1785/0220160221

Chiaraluce, L., Ellsworth, W. L., Chiarabba, C., & Cocco, M. (2003). Imaging the complexity of an active normal fault system: The 1997 Colfiorito (Central Italy) case study. *Journal of Geophysical Research - Solid Earth*, *108*(B6). https://doi.org/10.1029/2002JB002166

Chiaraluce, L., Valoroso, L., Piccinini, D., Di Stefano, R., & De Gori, P. (2011). The anatomy of the 2009 L'Aquila normal fault system (Central Italy) imaged by high resolution foreshock and aftershock locations. *Journal of Geophysical Research - Solid Earth*, *116*, B12311. https://doi.org/10.1029/2011JB008352

Cocco, M., Nostro, C., & Ekström, G. (2000). Static stress changes and fault interaction during the 1997 Umbria-Marche earthquake sequence. *Journal of Seismology*, *4*(4), 501–516.

Cultrera, G., Pacor, F., Franceschina, G., Emolo, A., & Cocco, M. (2009). Directivity effects for moderate-magnitude earthquakes (M_W 5.6–6.0) during the 1997 Umbria–Marche sequence, Central Italy. *Tectonophysics*, *476*(1–2), 110–120.

De Landro, G., Amoroso, O., Stabile, T. A., Matrullo, E., Lomax, A., & Zollo, A. (2015). High-precision differential earthquake location in 3-D models: Evidence for a rheological barrier controlling the microseismicity at the Irpinia fault zone in southern Apennines. *Geophysical Supplements to the Monthly Notices of the Royal Astronomical Society*, *203*(3), 1821–1831.

De Natale, G., Crippa, B., Troise, C., & Pingue, F. (2011). Abruzzo, Italy, earthquakes of April 2009: Heterogeneous fault-slip models and stress transfer from accurate inversion of ENVISAT-InSAR data. *Bulletin of the Seismological Society of America*, *101*(5), 2340–2354.

Di Domenica, A., Bonini, L., Calamita, F., Toscani, G., Galuppo, C., & Seno, S. (2014). Analogue modeling of positive inver- sion tectonics along differently oriented pre- thrusting normal faults: An application to the Central-Northern Apennines of Italy. *Geological Society of America Bulletin*, *126*(7-8), 943–955. https://doi.org/10.1130/B31001.1

Fréchet, J. (1985). *Sismogenése et doublets sismiques, thése d'Etat* (p. 206). Grenoble, France: Univ. é Sci. et Méd. de Grenoble.

Galadini, F., & Galli, P. (2000). Active tectonics in the central Apennines (Italy)–input data for seismic hazard assessment. *Natural Hazards*, *22*(3), 225–268.

Galli, P., Galderisi, A., Peronace, E., Giaccio, B., Hajdas, I., Messina, P., et al. (2019). The awakening of the dormant Mt Vettore fault (2016 central Italy earthquake, M_W 6.6). Paleoseismic clues on its millennial silences. *Tectonics*, *38*(2), 687–705. https://doi.org/10.1029/2018TC005326

Galli, P., Peronace, E., & Tertulliani, A. (2016). *Rapporto sugli effetti macrosismici del terremoto del 24 Agosto 2016 di Amatrice in scala MCS*, (p. 15). Roma: rapporto congiunto DPC, CNR-IGAG, INGV. https://doi.org/10.5281/zenodo.161323 (in Italian)

Hartzell, S. H., & Heaton, T. H. (1986). Rupture history of the 1984 Morgan Hill, California, earthquake from the inversion of strong motion records. *Bulletin of the Seismological Society of America*, *76*(3), 649–674.

Hernandez, B., Cocco, M., Cotton, F., Stramondo, S., Scotti, O., Courboulex, F., & Campillo, M. (2004). Rupture history of the 1997 Umbria-Marche (Central Italy) main shocks from the inversion of GPS, DInSAR and near field strong motion data. *Annals of Geophysics*, *47*(4), 1355–1376. https://doi.org/10.4401/ag-3349

Herrmann, R. B., Benz, H., & Ammon, C. J. (2011). Monitoring the earthquake source process in North America. *Bulletin of the Seismological Society of America*, *101*(6), 2609–2625.

Lavecchia, G., Ferrarini, F., Brozzetti, F., De Nardis, R., Boncio, P., & Chiaraluce, L. (2012). From surface geology to aftershock analysis: Constraints on the geometry of the L'Aquila 2009 seismogenic fault system. *Italian Journal of Geosciences*, *131*(3), 330–347.

Lomax, A., Zollo, A., Capuano, P., & Virieux, J. (2001). Precise, absoute earthquake location under Somma-Vesuvius volcano using a new 3D velocity model. *Geophysical Journal International*, *146*, 313–331.

Michele, M., Di Stefano, R., Chiaraluce, L., Cattaneo, M., De Gori, P., Monachesi, G., et al. (2016). The Amatrice 2016 seismic sequence: A preliminary look at the mainshock and aftershocks distribution. *Annals of Geophysics*, *59*.

Mildon, Z. K., Roberts, G. P., Faure Walker, J. P., & Iezzi, F. (2017). Coulomb stress transfer and fault interaction over millennia on non-planar active normal faults: The M w 6.5–5.0 seismic sequence of 2016–2017, Central Italy. *Geophysical Journal International*, *210*(2), 1206–1218.

Noda, H., & Lapusta, N. (2013). Stable creeping fault segments can become destructive as a result of dynamic weakening. *Nature*, *493*(7433), 518–521. https://doi.org/10.1038/nature11703

Nostro, C., Chiaraluce, L., Cocco, M., Baumont, D., & Scotti, O. (2005). Coulomb stress changes caused by repeated normal faulting earthquakes during the 1997 Umbria-Marche (Central Italy) seismic sequence. *Journal of Geophysical Research - Solid Earth*, *110*, B05S20. https://doi.org/10.1029/2004JB003386

Pace, B., Bocchini, G. M., & Boncio, P. (2014). Do static stress changes of a moderate-magnitude earthquake significantly modify the regional seismic hazard? Hints from the L'Aquila 2009 normal-faulting earthquake (M_W 6.3, Central Italy). *Terra Nova*, *26*(6), 430–439.

Papadopoulos, G. A., Ganas, A., Agalos, A., Papageorgiou, A., Triantafyllou, I., Kontoes, C., et al. (2017). Earthquake triggering inferred from rupture histories, DInSAR ground deformation and stress-transfer modelling: The case of Central Italy during august 2016–January 2017. *Pure and Applied Geophysics*, *174*(10), 3689–3711. https://doi.org/10.1007/s00024-017-1609-8

Pino, N. A., Mazza, S., & Boschi, E. (1999). Rupture directivity of the major shocks in the 1997 Umbria-Marche (Central Italy) sequence from regional broadband waveforms. *Geophysical Research Letters*, *26*(14), 2101–2104.

Pizzi, A., Di Domenica, A., Gallovič, F., Luzi, L., & Puglia, R. (2017). Fault segmentation as constraint to the occurrence of the main shocks of the 2016 Central Italy seismic sequence. *Tectonics*, *36*, 2370–2387.

Porreca, M., Minelli, G., Ercoli, M., Brobia, A., Mancinelli, P., Cruciani, F., et al. (2018). Seismic reflection profiles and subsurface geology of the area interested by the 2016–2017 earthquake sequence (Central Italy). *Tectonics*, *37*(4), 1116–1137. https://doi.org/10.1002/2017TC004915

Poupinet, G., Ellsworth, W. L., & Frechet, J. (1984). Monitoring veloc- ity variations in the crust using earthquake doublets: An application to the Calaveras Fault, California. *Journal of Geophysical Research*, *89*, 5719–5731. https://doi.org/10.1029/JB089iB07p05719

Pucci, S., De Martini, P. M., Civico, R., Villani, F., Nappi, R., Ricci, T., et al. (2017). Coseismic ruptures of the 24 August 2016, M_W 6.0 Amatrice earthquake (Central Italy). *Geophysical Research Letters*, *44*, 2138–2147.

Rovida, A., Locati, M., Camassi, R., Lolli, B., & Gasperini, P. (2019). Catalogo Parametrico dei Terremoti Italiani (CPTI15), *versione 2.0. Istituto Nazionale di Geofisica e Vulcanologia (INGV). Italy*. https://doi.org/10.13127/CPTI/CPTI15.2

Schaff, D. P., Bokelmann, G., Ellsworth, W. L., Zanzerkia, E., Waldhauser, F., & Beroza, G. C. (2004). Optimizing correlation techniques for improved earthquake location. *Bulletin of the Seismological Society of America*, *94*, 705–721. https://doi.org/10.1785/0120020238

Schaff, D. P., Bokelmann, G. H., Beroza, G. C., Waldhauser, F., & Ellsworth, W. L. (2002). High-resolution image of Calaveras fault seismicity. *Journal of Geophysical Research - Solid Earth*, *107*(B9), ESE-5), ESE 5-1–ESE 5-16. https://doi.org/10.1029/2001JB000633

Schaff, D. P., & Waldhauser, F. (2005). Waveform cross-correlation-based differential travel-time measurements at the northern California seismic network. *Bulletin of the Seismological Society of America*, *95*(6), 2446–2461.

Scognamiglio, L., Tinti, E., Casarotti, E., Pucci, S., Villani, F., Cocco, M., et al. (2018). Complex Fault Geometry and Rupture Dynamics of the M_W 6.5, 30 October 2016, Central Italy earthquake. *Journal of Geophysical Research: Solid Earth*, *123*(4), 2943–2964.

Scognamiglio, L., Tinti, E., & Michelini, A. (2009). Real-time determination of seismic moment tensor for the Italian region. *Bulletin of the Seismological Society of America*, *99*(4), 2223–2242.

Serpelloni, E., Anzidei, M., Baldi, P., Casula, G., & Galvani, A. (2005). Crustal velocity and strain-rate fields in Italy and surrounding regions: New results from the analysis of permanent and non-permanent GPS networks. *Geophysical Journal International*, *161*(3), 861–880.

Tinti, E., Scognamiglio, L., Michelini, A., & Cocco, M. (2016). Slip heterogeneity and directivity of the ML 6.0, 2016, Amatrice earth- quake estimated with rapid finite-fault inversion. *Geophysical Research Letters*, *43*, 10,745–10,752. https://doi.org/10.1002/2016GL071263

Valoroso, L., Chiaraluce, L., Piccinini, D., Di Stefano, R., Schaff, D., & Waldhauser, F. (2013). Radiography of a normal fault system by 64,000 high-precision earthquake locations: The 2009 L'Aquila (Central Italy) case study. *Journal of Geophysical Research: Solid Earth*, *118*, 1156–1176.

Verdecchia, A., Pace, B., Visini, F., Scotti, O., Peruzza, L., & Benedetti, L. (2018). The role of viscoelastic stress transfer in long-term earthquake cascades: Insights after the Central Italy 2016–2017 seismic sequence. *Tectonics*, *37*(10), 3411–3428.

Villani, F., Civico, R., Pucci, S., Pizzimenti, L., Nappi, R., De Martini, P. M., et al. (2018). A database of the coseismic effects following the 30 October 2016 Norcia earthquake in Central Italy. *Scientific data*, *5*(1), 180049. https://doi.org/10.1038/sdata.2018.49

Vuan, A., Sugan, M., Chiaraluce, L., & Di Stefano, R. (2017). Loading rate variations along a midcrustal shear zone preceding the M_W6. 0 earthquake of 24 August 2016 in Central Italy. *Geophysical Research Letters*, *44*, 12–70. https://doi.org/10.1002/2017GL076223

Waldhauser, F. (2001). hypoDD: A program to compute double-difference hypocenter locations, U.S. Geological Survey Open-File Report, 01–113.

Waldhauser, F. (2009). Near-real-time double-difference event location using long-term seismic archives, with application to northern California. *Bulletin of the Seismological Society of America*, *99*(5), 2736–2748. https://doi.org/10.1785/0120080294

Waldhauser, F., & Ellsworth, W. L. (2000). A double-difference earthquake location algorithm: Method and application to the northern Hayward Fault, California. *Bulletin of the Seismological Society of America*, *90*, 1353–1368. https://doi.org/10.1785/0120000006

Waldhauser, F., & Schaff, D. P. (2008). Large-scale relocation of two decades of Northern California seismicity using cross-correlation and double-difference methods. *Journal of Geophysical Research*, *113*, B08311. https://doi.org/10.1029/2007JB005479

Xu, G., Xu, C., Wen, Y., & Jiang, G. (2017). Source parameters of the 2016–2017 Central Italy earthquake sequence from the Sentinel-1, ALOS-2 and GPS data. *Remote Sensing*, *9*(11), 1182.